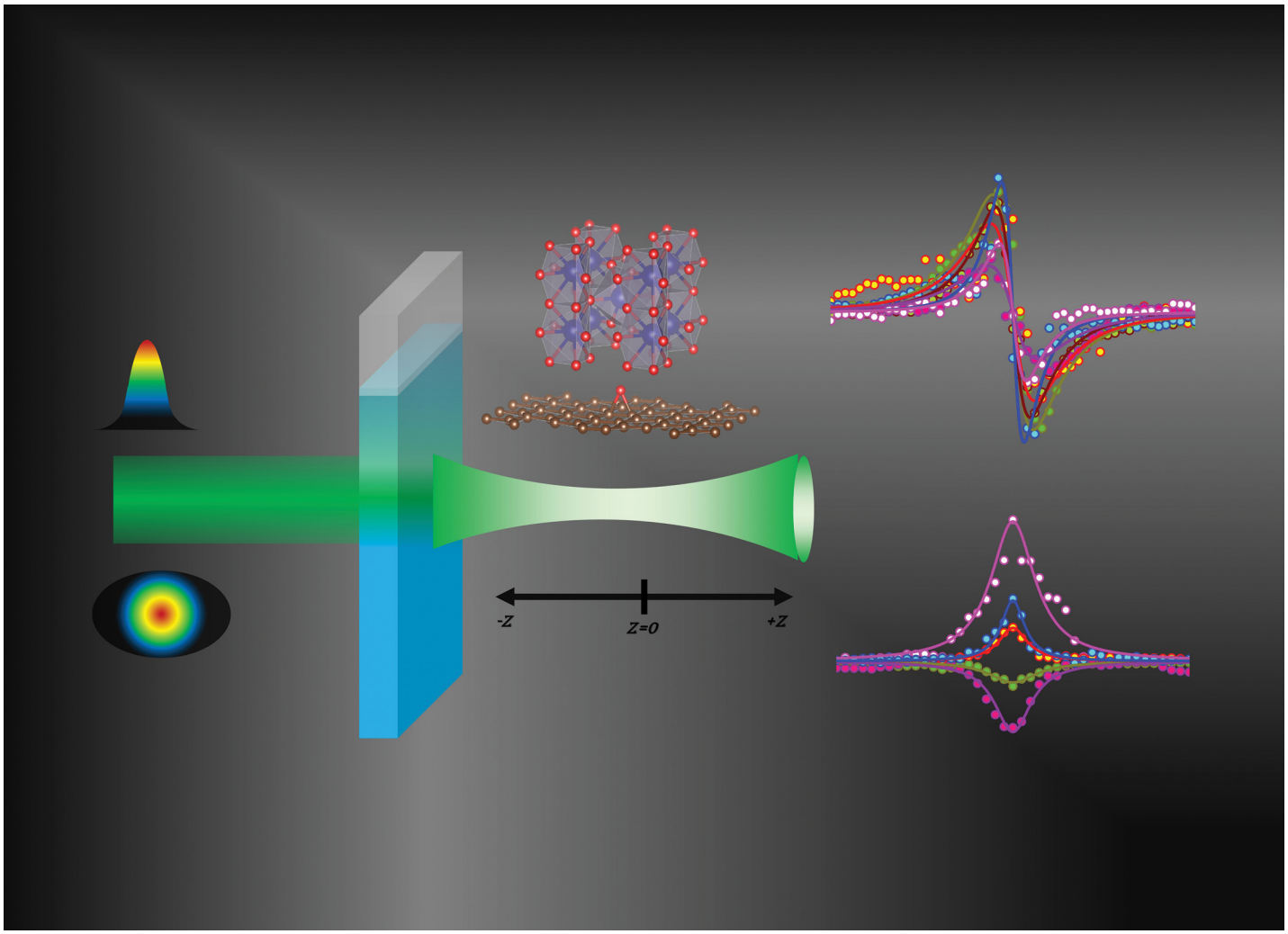

Showcasing research from Professor Ishtiaque M. Syed's laboratory, Department of Physics, University of Dhaka, Dhaka, Bangladesh.

Tuning the nonlinear optical properties of SnO_2–rGO nanocomposites: exploration using conventional Z-scan and thermal lensing models

In this work, we synthesized SnO_2 and GO to produce SnO_2–rGO nanocomposites of different ratios. After careful investigation of the nanocomposites, we compared their nonlinear optical (NLO) properties, which pave the way for the optimization of SnO_2–rGO nanocomposites for applications in optical limiters, mode-locking laser systems, switchers, and other nonlinear photonic devices, contributing to the development of more efficient materials in modern optics.

Image reproduced by permission of Md Kamal Uddin, Pulak Das Gupta and Suptajoy Barua from *Mater. Adv.*, 2025, **6**, 9407.

As featured in:

See Md Kamal Uddin *et al.*, *Mater. Adv.*, 2025, **6**, 9407.

ROYAL SOCIETY OF CHEMISTRY

rsc.li/materials-advances

Registered charity number: 207890

Materials Advances

ROYAL SOCIETY OF CHEMISTRY

PAPER

View Article Online
View Journal | View Issue

Cite this: *Mater. Adv.*, 2025, 6, 9407

Tuning the nonlinear optical properties of SnO_2–rGO nanocomposites: exploration using conventional Z-scan and thermal lensing models

Pulak Das Gupta, [a] Md Kamal Uddin, *[a] Suptajoy Barua, [a] Umma Sumaia Akter Meem, [a] Md. Jubair Ahmed Sourov, [b] Tanvir Ahmed, [a] Md Wahadoszamen, [a] Rumana A. Jahan [c] and Ishtiaque M. Syed [a]

This study investigates the nonlinear optical properties of SnO_2–rGO nanocomposites by employing a conventional Z-scan technique and a thermal lensing model using a CW laser with an excitation wavelength of 532 nm. The fabrication of three batches of SnO_2–rGO nanocomposites at three compositional ratios 1 : 1, 1.25 : 1, and 2.5 : 1 (three different concentrations for each), was achieved *via* a conventional hydrothermal method followed by chemical reduction. The fabricated samples were subjected to rigorous investigations and analyses using UV-visible spectroscopy, XRD, FESEM, Raman spectroscopy, FTIR, and photoluminescence (PL) methods to uncover precisely their morphological details, sizes, defects, charge transfer characteristics, and identities. At low intensity (I_0 = 1.0 kW cm^{-2}), our open aperture (OA) data suggest that both SnO_2 and GO exhibit reverse saturation absorption (RSA), whereas rGO and SnO_2–rGO nanocomposites show tunable saturation absorption (SA) characteristics. But at a higher intensity (I_0 = 5.3 kW cm^{-2}), the symmetrical nature of all the close aperture (CA) data suggests that at this intensity, the nonlinear refraction dominated, and the values of the nonlinear refractive index were found to be negative, indicating self-defocusing phenomena. We believe that the charge transfer mechanism and the induced defect state can play dominant roles in tuning the nonlinear optical characteristic of the nanocomposites. A DFT study also uncovers further theoretical insight into the charge transfer characteristic in SnO_2–rGO nanocomposites.

Received 21st July 2025,
Accepted 7th August 2025

DOI: 10.1039/d5ma00790a

rsc.li/materials-advances

1. Introduction

Nonlinear optical properties of materials have attracted significant attention in recent years due to their potential applications in fields such as optical fiber communication systems,[1] optical signal processing,[2] optical limiters,[3] ultrafast switching devices,[4] mode-locking lasers,[5] logic gate devices,[6] saturable absorbers,[7] two-photon imaging and microscopy,[8] optical modulators,[9] and nanophotonics devices.[10,11] Among these, the third-order nonlinear optical phenomena are the most significant and dominating nonlinear properties, which also play a major role in understanding light–matter interactions.[12,13] These third-order nonlinear phenomena encircle significant effects such as third harmonic generation,[14] the Kerr effect,[15] thermal effect,[16] Stark effect,[17] and self-focusing or defocusing.[18,19] For this reason, third-order optical nonlinearity has been extensively investigated in various materials, ranging from metals,[20] semimetals,[21] semiconductors,[22] organic materials,[23] and topological materials.[24] In particular, graphene and graphene-based materials exhibit good third-order nonlinear optical responses.[25,26] Graphene has been considered a highly promising material for broadband optical nonlinear devices, such as saturable absorbers (SA),[27] optical limiters,[28] and modulators[29] due to its broad absorption spectrum,[30] ultrafast carrier dynamics,[31] and band-filling effects.[32] Graphene oxide (GO), a significant related material in the graphene family, also exhibits significant nonlinear optical characteristics.[33] Its electronic band structure can be varied over a wide range by changing the amount and reduction of different types of oxygen-containing functional groups, such as epoxides, hydroxyls, and carboxyls, on its basal plane and edges.[34] The band gap of GO ranges from 2.2 to 0.5 eV,[35] indicating that transitions from insulator to semiconductor and then to semimetal may also be possible.[36] Moreover, GO has some characteristics of graphene due to the presence of pristine graphitic nanoislands, and the reduction of GO can almost restore the physical structure of pristine graphene.[37,38] After reducing the oxygen functional group of GO, sp^3-hybridized carbons, largely present in GO, are converted into sp^2-hybridized carbons. This turns GO

[a] *Department of Physics, University of Dhaka, Dhaka-1000, Bangladesh. E-mail: kamal@du.ac.bd*
[b] *Department of Robotics and Mechatronics Engineering, University of Dhaka, Dhaka-1000, Bangladesh*
[c] *Centre for Advanced Research in Sciences, University of Dhaka, Dhaka-1000, Bangladesh*

into reduced graphene oxide (rGO) and decreases O/C ratios, indicating the reduction of more oxygen functional groups in GO. Due to the restoration of sp^2 sites in the structure, the optical properties of rGO are significantly modified.[38,39] The physical properties of rGO lie between GO and pristine graphene. The nonlinear optical properties of GO and rGO, including their two-photon absorption (TPA) properties as well as saturable absorption (SA) phenomena, make them promising candidates as optical limiters and saturable absorbers.[40,41] On the other hand, other semiconducting materials with relatively wide band gaps exhibit weak nonlinear responses, even under very strong optical fields. The narrow band gap materials produce a much larger nonlinear response than larger band gap semiconductors such as SnO_2.[42] For instance, materials with large nonlinear absorption coefficients and refractive indices that can be activated at low intensities are highly in demand for photonics and optoelectronics applications. Two effective processes to explain large third-order nonlinearities are the photoinduced charge transfer of a donor–acceptor pair complex[43–46] and induced defect states in nanocomposites.[47–50] As rGO has a very low bandgap, it has better nonlinearity than any other wider band gap semiconductor, for example SnO_2. Thus, it is possible to tune the nonlinear optical properties of SnO_2–rGO nanocomposites (treating it as a donor–acceptor or acceptor–donor) due to the efficient charge transfer characteristic. Along with charge transfer, in nanocomposites, defect states also play a crucial role. A decrease in the density of the localized defect states in nanostructures causes tunable saturable absorption (SA) or one-photon absorption (OPA) with a low saturation intensity threshold. On the other hand, with the increase of the localized defect density, SA can be reduced, and reverse saturation absorption (RSA) becomes dominant.[51,52] These localized defect states can significantly alter the band gap energy in the nanocomposites,[53] and improve the nonlinear optical properties of SnO_2–rGO nanocomposites as potential candidates in photonic devices.

There are studies on investigating the nonlinear optical (NLO) properties involving GO, rGO, and rGO-based nanocomposites through both pulse and continuous wave (CW) lasers using the Z-scan technique. For instance, Shilpa *et al.*[54] investigated the NLO properties of noble metal decorated rGO and Ti_3C_2 MXene *via* Z-scan measurements by utilizing a CW diode laser irradiating at 532 nm. They harnessed the open aperture Z-scan data to reveal the RSA behavior in rGO, Ti_3C_2, and their nanocomposites with noble metals and showed that such formation of nanocomposites *via* initial reduction of GO to rGO notably enhances the NLO properties as well as the optical limiting performance. Saravanan *et al.*[55] demonstrated enhanced third-order NLO properties and optical limiting behavior of hydrothermally synthesized zinc ferrite decorated rGO nanohybrids under both CW (532 nm, 50 mW) and ultrafast (800 nm, 150 fs) laser excitation. They attributed the enhancement to a synergistic effect and the creation of defect-induced states upon decoration. Several other studies were also performed, showing the importance of charge transfer phenomena and the effect of localized defect states in improving the third-order NLO properties of GO/rGO-based nanocomposites.[37,46,56–58]

While CW and pulsed lasers provide complementary insights into NLO properties, the investigation of NLO properties of nanocomposites using CW laser systems remains largely unexplored. Given the widespread use of CW lasers across various applications, with power levels ranging from μW to kW, protecting the human eye and optical sensors has become crucial. Since the human eye has its peak spectral sensitivity in the green region, and green CW lasers are commonly used in interactive environments, optical limiters are essential to ensure safety. Since the thermal nonlinearity and RSA phenomena predominately occur in the CW regime of laser light, it is important to investigate both the thermal lensing effect and the conventional Z-scan model.

In this study, SnO_2–rGO nanocomposites present a fascinating platform for studying and tuning the nonlinear optical responses, offering a potential pathway for designing materials with optimized performance for specific applications. This research investigates the nonlinear optical properties of SnO_2–rGO nanocomposites, focusing on the effects of varying concentrations of GO and SnO_2 on their nonlinear optical response. In this study, both conventional Z-scan and thermal lensing models are used to analyze the nonlinear absorption and refraction or lensing properties of the SnO_2–rGO nanocomposites, providing insights into their potential for use in practical optical devices and photonics technology. By exploring the interplay between these two components and their impact on nonlinear optical behavior, this work aims to contribute to the design and development of advanced nano-materials with tunable optical properties for future photonic applications.

2. Methodology

2.1 Materials and reagents

Tin chloride dihydrate ($SnCl_2{\cdot}2H_2O$) and phosphoric acid (extra pure) were purchased from Sisco Research Laboratories Pvt. Ltd. Sulfuric acid (98% pure) and ethanol (extra pure) were purchased from Merck KGaA, 25 064 293 Darmstadt. Loba Chemie Pvt. Ltd supplied NaOH (98% pure), and Sigma-Aldrich provided graphite powder and potassium permanganate (extra pure). These reagents were used directly out of the package without modification. For washing purposes at various stages, we used de-ionized and nano-pure water.

2.2 Synthesis of graphene oxide (GO) and reduced graphene oxide (rGO)

Graphene oxide was synthesized using the improved Hummers' method.[59,60] First, H_2SO_4 and H_3PO_4 acids were mixed in a beaker at a ratio of 9 : 1, into which 2 g of graphite powder was dissolved with vigorous stirring, followed by the addition of 6 g of $KMnO_4$. After that, the solution was kept at 50 °C with strong magnetic stirring for 2 hours. The solution was then poured into a beaker filled with ice of nano pure water, and then 10 ml of 30% H_2O_2 was added slowly to the solution with slow stirring to mix well. The mixture was then centrifuged at 7000 rpm at 5 °C for 15 minutes, and the precipitate was washed 5 times with DI

water and several times with HCl, respectively. The collected precipitate was then washed with DI water several times until Cl^- ions were completely discarded from the solution (confirmed by a Cl^- ion test). The collected precipitate was further washed with ethanol and dried in a vacuum drier.[60] Finally, to obtain rGO for a comparative study, some of the dried sample was subjected to thermal treatment in a furnace at 200 °C for 5 hours. This step effectively reduced GO to reduced graphene oxide (rGO) and stabilized the composite structure.[61]

2.3 Synthesis of SnO_2

Tin oxide (SnO_2) nanoparticles were synthesized using the conventional hydrothermal method.[62] Initially, 50 mL of a 1 M solution of tin chloride dihydrate ($SnCl_2{\cdot}2H_2O$) and 10 mL of a 1 M solution of sodium hydroxide (NaOH) were prepared. The NaOH solution was then added dropwise to the tin chloride solution under constant stirring, producing a white precipitate of tin hydroxide ($Sn(OH)_2$). After completely adding NaOH, 40 mL of nano-pure water was added to the mixture, ensuring thorough mixing. The solution was then transferred to a hydrothermal reactor and heated at 100 °C for 12 hours to ensure further reaction and crystallization. During the hydrothermal process, the precipitated $Sn(OH)_2$ decomposed to form SnO, which was further oxidized to SnO_2 in the presence of dissolved oxygen. The resulting mixture was cooled to room temperature, and the obtained precipitate was centrifuged and washed several times (fifteen times) with nano-pure water under a 15 000-rpm centrifuge to remove any residual byproducts such as NaCl. Finally, the washed nanoparticles were dried in an oven at 100 °C for several hours and then calcined at 400 °C for 2 hours to enhance their crystallinity and stability.

2.4 Preparation of SnO_2–rGO compound solution

The synthesis of SnO_2-reduced graphene oxide (rGO) nanocomposites was initiated by dispersing 1 g of GO in 240 mL of ethanol. The solution was stirred thoroughly to achieve a uniform distribution of the GO sheets. After achieving appropriate dispersion, specific amounts of SnO_2 nanoparticles—1 g, 1.25 g, and 2.5 g, respectively—were added to prepare nanocomposites with three different weight ratios of SnO_2 : GO (1 : 1, 1.25 : 1, and 2.5 : 1). The mixtures were stirred for 1 hour to ensure homogenous blending of SnO_2 nanoparticles with GO. The mixtures were then transferred into Teflon-lined autoclave vessels, sealed tightly, and heated at 200 °C for 5 hours under hydrothermal conditions to reduce GO to rGO (shown in Fig. 1). This process facilitated strong interactions between the SnO_2 nanoparticles and rGO. After the reaction, the vessels were allowed to cool naturally to room temperature, and as before, the obtained precipitate was centrifuged and washed several times (fifteen times) with nano-pure water.[63]

2.5 Characterization techniques

The UV-visible absorption spectra for all the prepared dispersion samples were measured using a Shimadzu UV-1800 spectrophotometer. The measurements were taken in a 4 ml quartz cuvette with a 1 cm path length, covering a wavelength range

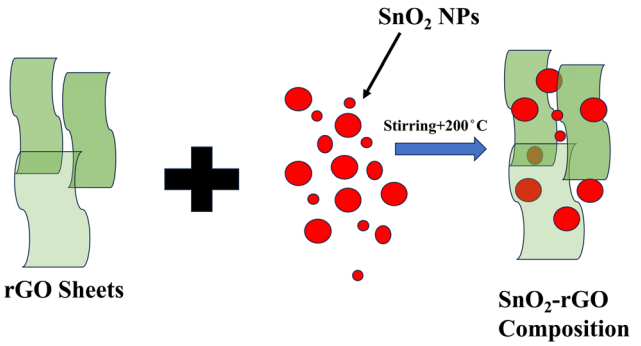

Fig. 1 Schematic diagram of the formation of SnO_2–rGO nanocomposites.

from 190 to 1100 nm. The morphology and size of the nanoparticles were examined using a field emission scanning electron microscope (FESEM) (ZEISS Sigma 300) operating (with a resolution of 10 nm) at an accelerating voltage of 15 kV and an X-ray diffractometer (Rigaku Ultima IV) with a copper target of wavelength 1.5406 Å. Fourier transform infrared (FTIR 8400S) spectroscopy for the 400 cm^{-1} to 4000 cm^{-1} wavenumber range was carried out to identify the functional groups. The Raman spectra of the samples were recorded using a Horiba Macro-RAM™ high-resolution Raman spectrometer equipped with a 785 nm diode laser. The spectrometer features a flat-field output spectrograph with a single aberration-corrected concave grating and a 120 mm focal length. The probe head, designed with a headspace focal length of approximately 4 cm, enhances signal collection and incorporates high-performance Raman edge filters. All Raman measurements in this study were carried out using a steady laser excitation power of around 5 mW on the sample surface, with a fixed acquisition time of 5 seconds and the same number of accumulations for each scan.

2.6 Z-scan measurement

The experimental Z-scan setup is shown in the schematic diagram in Fig. 2. In the investigation, a low-power continuous wave diode laser with the 532 nm laser line is used as the excitation light source. The beam is focused onto a point ($z = 0$) along the scan axis (z-axis) using a biconvex lens ($f = 100$ mm). The spot size ($2w_0$) at the focus of the lens is estimated to be 43.6 μm. So, the value of the Rayleigh length for our Z-scan setup is estimated ($z_0 = \pi w_0^2/\lambda$) to be 2.8 mm, greater than the sample quartz cuvette (1 mm). The sample is positioned on an x–y–z stage that moves back and forth along the z-axis, starting from the focal point ($z = 0$) of the beam. As the sample moves in steps from the lens side toward the detector side, passing through the focus, the transmitted intensity at each position is measured and recorded using a computer-controlled detector.

The standard Z-scan technique, originally developed by Sheik-Bahae *et al.*[64,65] offers an effective and precise method for determining both the sign and magnitude of the nonlinear refractive index n_2, as well as the nonlinear absorption coefficient β. This model assumes a local interaction between the electromagnetic field and the material, where the sample's susceptibility depends solely on the local intensity. Consider

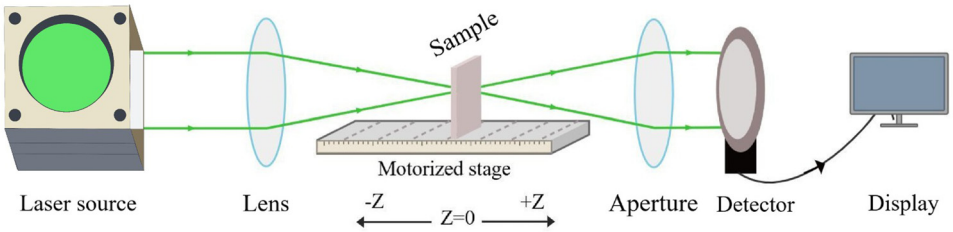

Fig. 2 Schematic diagram of the Z-scan setup.

a TEM_{00} Gaussian beam with a beam waist w_0 propagating in the $+z$ direction, the electric field $E(z, r, t)$ can be expressed as:

$$E(z,r,t) = E_0(t)\frac{w_0}{w(z)}\exp\left(-\frac{r^2}{w^2(z)} - \frac{ikr^2}{2R(z)}\right)e^{-i\phi(z,t)} \quad (1)$$

Here, $w(z) = w_0\{1 + (z/z_0)^2\}^{1/2}$ is the beam radius, $R(z) = z(1 + (z/z_0)^2)$ is the radius of curvature of the wave front at z, w_0 is the beam waist at $z = 0$, $z_0 = kw_0^2/2$ is the Rayleigh length, $k = 2\pi/\lambda$ is the wave vector, λ is the wavelength of the laser source in free space, and $r(x, y)$ is the transverse radial distance. The term $E_0(t)$ represents the electric field at the focal point and includes the temporal shape (or envelope) of the laser pulse. Meanwhile, the exponential term $e^{-i\phi(z,t)}$ accounts for all uniform phase shifts that do not vary with radial position. Under the thin sample approximation, the amplitude of the electric field and the nonlinear phase shift, denoted as $\Delta\phi$, are described by the following two coupled equations.

$$\frac{d\Delta\phi}{dz'} = k\Delta n(I) \text{ and } \frac{dI}{dz'} = -\alpha(I)I \quad (2)$$

where z' is the propagation depth in the sample, and the total absorption coefficient, $\alpha(I) = \alpha + \beta(I)I$, where, α is the linear absorption coefficient and $\beta(I)$ is the nonlinear absorption coefficient of the sample. Meanwhile, the overall refractive index, denoted as $n(I)$, depends on the laser intensity and can be described using the nonlinear refractive index n_2. It is given by the formula $n(I) = n_0 + n_2(I)I$, where n_0 is the linear refractive index, and I represents the intensity of the laser beam inside the sample. When nonlinear absorption is negligible (*i.e.*, $\beta = 0$), the normalized transmittance in the close-aperture (CA) Z-scan setup, $T(z)$, can be calculated using the following expression.

$$T(z) = 1 + \frac{4\Delta\phi_0\left(\frac{z}{z_0}\right)}{\left[1 + \left(\frac{z}{z_0}\right)^2\right]\left[9 + \left(\frac{z}{z_0}\right)^2\right]} \quad (3)$$

The peak-to-valley difference in the close-aperture (CA) Z-scan curve, represented as $(\Delta T_{p\text{-}v})$ is directly related to the nonlinear phase shift $\Delta\phi_0$ and follows an almost linear relationship when the phase shift is small ($|\Delta\phi_0| \leq \pi$). This relationship is given by the equation: $\Delta T_{p\text{-}v} = 0.406\ (1 - s)^{0.25}|\Delta\phi_0|$. Here, s is the linear transmittance of the aperture.[64,65] According to the Sheik-Bahae formalism (SBF), the distance between the peak and valley positions along the z-axis is approximately: $\Delta z_{p\text{-}v} = 1.7z_0$. This spatial separation is a signature of third-order (cubic) nonlinearity in the sample.[64,65] But for a high nonlinear phase-shift, $\Delta T_{p\text{-}v}$ in the normalized CA Z-scan curves follows the equation, $\Delta T_{p\text{-}v} = 3.06\ (1 - e^{-|\Delta\phi_0|/5.81})\ (1 - s)^{0.25}$ for $|\Delta\phi_0| < 25$.[66] This equation shows that a higher phase shift $(\Delta\phi_0)$ results in a larger peak-to-valley difference in the CA curve. It is also worth noting that when there is no significant nonlinear absorption, the CA Z-scan curve remains symmetric as the sample moves along the z-axis ($z \to \pm\infty$). However, if nonlinear absorption is present, the symmetry of the curve breaks.[67–73] But for the laser beam with circular symmetry and low power intensities including the contributions of nonlinear absorption or two-photon absorption (TPA), the normalized transmittance $T(z)$ is used which is written as,[69,70,74] $T(z) = 1 + T_{\Delta\phi}(z) + T_{\Delta\psi}(z)$, here, $T_{\Delta\phi}(z)$ and $T_{\Delta\psi}(z)$ are generated by induced nonlinear refraction and nonlinear absorption or induced TPA, respectively. These two terms can be separately used for close-aperture (pure nonlinear refraction (NLR)) and open-aperture (pure nonlinear absorption (NLA)) experiments, and the separate equations for the pure NLR (close aperture) and TPA (open aperture) are

$$T_{\Delta\phi}(z) = 1 + \frac{4\Delta\phi_0\left(\frac{z}{z_0}\right)}{\left[1 + \left(\frac{z}{z_0}\right)^2\right]\left[9 + \left(\frac{z}{z_0}\right)^2\right]} \quad (4a)$$

$$T_{\Delta\psi} = 1 - \frac{\Delta\psi_0}{\sqrt{2}\left[\left(\frac{z}{z_0}\right)^2 + 1\right]} \quad (4b)$$

where $\Delta\phi_0$ is the nonlinear phase shift, and $\Delta\psi_0$ is the two-photon induced absorption. The nonlinear refractive index n_2 and nonlinear absorption coefficient β can be estimated from the following relationships

$$n_2 = \frac{\Delta\phi_0}{kI_0L_{eff}} \quad (5a)$$

$$\beta = \frac{2\Delta\psi_0}{I_0L_{eff}} \quad (5b)$$

where, I_0 stands for the on-axis input intensity at the focus, $L_{eff} = (1 - e^{-\alpha L})/\alpha$ is the effective length, and L is the geometrical length of the sample.[64,65,69,70]

Now, considering that both the SA and TPA contribute to the absorption response in Z-scan measurements, we can write[13]

$$\alpha(I) = \frac{\alpha}{1 + \frac{I}{I_{sat}}} + \beta I \quad (6)$$

where I_{sat} is the saturable intensity and I is related to the optical peak intensity at the focus I_0, the Rayleigh length z_0 of the beam and the sample position z by, $I(z) = I_0/(1 + (z/z_0)^2)$. According to the expressions above, the normalized transmittance for an OA can be given by

$$T(z) = \left[1 - \frac{\alpha I_{sat} L}{I_{sat} + I_0 \Big/ \left(1 + \frac{z^2}{z_0^2}\right)} - \frac{\beta I_0 L}{1 + \frac{z^2}{z_0^2}}\right] \Big/ (1 - \alpha L) \quad (7)$$

The imaginary parts of the third-order susceptibility $\chi^{(3)}$ can be calculated using the relationship: Im $\chi^{(3)}$(esu) = $(10^{-7} c^2 n_0^2 \beta)/(96\pi^2\omega)$(cm W^{-1}), where c is the speed of light in cm s^{-1}, ω is the excitation frequency in s^{-1} and n_0 is the linear refractive index.[75]

The thermal-lens model (TLM) was investigated by Gordon *et al.*,[76] Sheldon *et al.*,[77] Carter *et al*,[78] and Cuppo *et al.*[71] When a Gaussian beam propagates through a weakly adsorbed medium, light is immediately absorbed, which causes local heating, produces heat diffusion along the radial direction, and gives rise to a spatially varying temperature field, *i.e.*, temperature gradient. This temperature field is not proportional to the local light intensity, and the refractive index of the medium is assumed to be a function of temperature. For small temperature changes ΔT, the refractive index change is proportional to ΔT and the rate of change of the total refractive index with temperature is $\partial n/\partial T$.[71,76,79] It means this thermal nonlinearity is due to the nonlocal dependence of the refractive index on the light intensity. The time dependence for far-field on-axis transmittance due to the thermal lensing effect is given as

$$T(z,t) = \frac{1}{1 + \left(\frac{\theta}{1 + \frac{t_c}{2t}}\right) \frac{2\left(\frac{z}{z_0}\right)}{1 + \left(\frac{z}{z_0}\right)^2} + \left(\frac{\theta}{1 + \frac{t_c}{2t}}\right)^2 \frac{1}{1 + \left(\frac{z}{z_0}\right)^2}} \quad (8)$$

where the thermal-diffusion time t_c is given by $t_c = w^2/4D$, $w = w_0\sqrt{1 + (z/z_0)^2}$ is the beam waist, $D = \kappa/C_\rho$ is the thermal diffusivity, C_ρ is the specific heat per volume at constant pressure, and κ is the thermal conductivity. At $t \gg t_c$, the steady state has been reached, and it can be expressed as

$$T(z) = \frac{1}{1 + \theta \frac{2\left(\frac{z}{z_0}\right)}{1 + \left(\frac{z}{z_0}\right)^2} + \theta^2 \frac{1}{1 + \left(\frac{z}{z_0}\right)^2}} \quad (9)$$

The thermal nonlinear refractive index n_2^{th} can be obtained using the on-axis thermally induced phase shift θ, *via*

$$n_2^{th} = \frac{\theta}{k I_0 L_{eff}} \quad (10)$$

and when thermal nonlinearity dominates, the separation between the peak to valley position in the CA Z-scan curve becomes, $\Delta z_{p-v} > 1.7 z_0$ which was even found to be greater than $2z_0$ or equal to $3.4z_0$.[65,71,78,80]

2.7 Computational details

The simulations in this study were performed using the Vienna *ab initio* Simulation Package (VASP), which is based on the density functional theory (DFT) approach.[81–84] The calculations used projector augmented wave (PAW) pseudopotentials, along with the generalized gradient approximation (GGA) for the exchange–correlation functional.[85,86] To maintain reliable accuracy in our calculations, we used a plane-wave cut-off energy of 530 eV. Geometry optimization was performed using the conjugate gradient method, with convergence criteria set to 0.01 eV Å^{-1} for forces and 10^{-8} eV for energy. For Brillouin-zone sampling, we applied a 14 × 8 × 1 *k*-point mesh based on the Monkhorst–Pack scheme.[87] Grimme's DFT-D2 correction was employed to account for the weak van der Waals interactions present between the layers of the heterostructure.[88]

3. Results and discussion

3.1 UV analysis

As shown in Fig. 3, the optical absorption spectrum of GO reveals the three absorption peaks at 232 nm, 307 nm, and 364 nm. The most intense band at 232 nm is due to a typical π–π* transition in aromatic C–C bonds, and the latter two correspond to the n to π* transition of the carbonyl (C═O) group, and are related to the hyperfine structures of the absorption spectrum of GO.[26,45,89] On the other hand, the peak of the π–π*

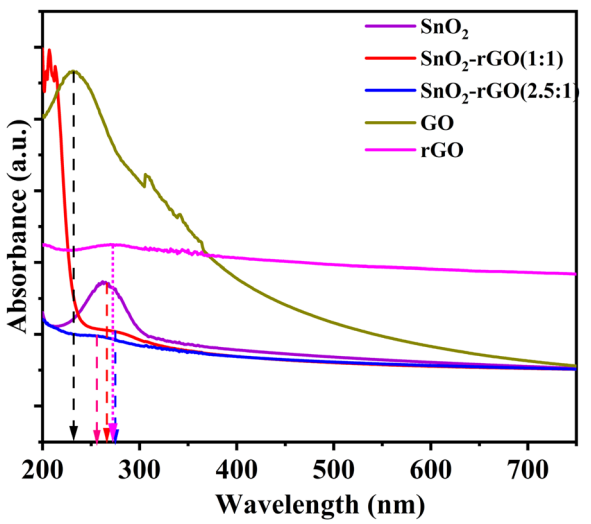

Fig. 3 Exploring optical properties of SnO_2, GO, rGO, and SnO_2–rGO nanocomposites through UV-vis spectroscopy.

transitions shifts to around 268 nm for rGO, indicating that some oxygen functional groups on the GO surface are removed and the conjugated structure is restored.[90,91] In contrast, pure SnO_2 exhibits an absorption peak at 266 nm, and shows a blueshift for SnO_2–rGO (2.5 : 1) and redshift for SnO_2–rGO (1 : 1) with the addition of rGO into the SnO_2 matrix. In both SnO_2 and SnO_2–rGO nanocomposite (NC) samples, the absorption peaks in the region of 266 nm correspond to band-to-band absorption in SnO_2, but in the spectrum of the SnO_2–rGO (2.5 : 1) NCs, there is a small absorption peak at 253 nm related to sp^2-hybridized rGO.[92,93] Moreover, the observed peak shift may be due to the composition of rGO with SnO_2 nanoparticles and related to the change in bandgap energy, probably due to the addition of rGO to the SnO_2 lattice structures, inducing the impurities in energy levels.

3.2 XRD analysis

The XRD patterns of SnO_2 were analyzed using the Rietveld refinement technique with $R_p = 16.5$, $R_{wp} = 24.5$ and $\chi^2 = 1.0064$, as shown in Fig. 4, revealing distinct diffraction peaks corresponding to the tetragonal rutile structure of SnO_2, confirming the successful synthesis of SnO_2 nanoparticles compared with JCPDS Card No. 41-1445.[94] The presence of its characteristic peaks in the XRD patterns of all samples (Fig. 4) suggests that the basic crystalline structure remains intact even after the incorporation of graphene oxide (later turned into rGO). These observations confirm that the synthesis method employed was successful in producing high-quality SnO_2 and SnO_2–rGO nanocomposites. Despite the retention of the tetragonal rutile structure, the intensity of the diffraction peaks decreases, and the peaks broaden as the rGO content increases, indicating that the interaction between SnO_2 and rGO inhibits the growth of the SnO_2 particles and reduces in crystallite size. The crystallite size of the SnO_2 and SnO_2–rGO nanocomposites was calculated using the Debye–Scherrer equation, and the results are summarized in Table 1. The presence of rGO sheets in the composite prevents particle agglomeration and enhances the dispersion of SnO_2 nanoparticles, leading to a more uniform distribution of particles.

3.3 FESEM analysis

The FESEM image of pure SnO_2 and SnO_2–rGO (Fig. 5) shows excellent dispersion of SnO_2 NPs in the SnO_2–rGO NCs samples. Pure SnO_2 NPs exhibit an agglomerated structure with spherical or near-spherical morphology. The agglomeration observed in pure SnO_2 is likely due to strong interparticle interactions, including van der Waals forces and hydrogen bonding, commonly present in metal oxide nanoparticles synthesized in aqueous media.[95] The average particle size of pure SnO_2 is observed at nearly 60 nm, which is consistent with the X-ray diffraction (XRD) results, confirming the small crystallite size of SnO_2. The agglomerated morphology of pure SnO_2 can limit the availability of active sites, hence impeding the transport of charge carriers. In contrast, the SnO_2–rGO nanocomposites exhibit a significantly different morphology with a reduced mean particle size. The FESEM images reveal that the

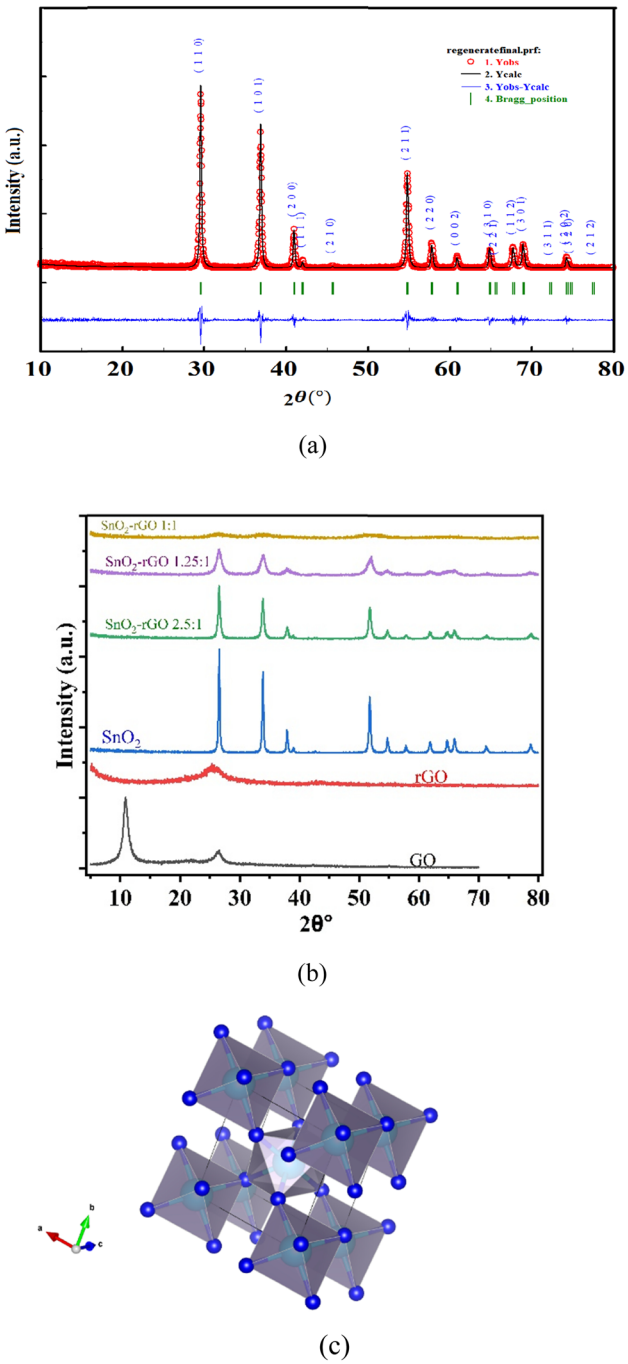

Fig. 4 (a) Rietveld analysis of SnO_2 nanoparticles; (b) room-temperature X-ray diffraction patterns of SnO_2, GO, rGO, and SnO_2–rGO all nanocomposites; (c) structural model of SnO_2.

Table 1 Structural properties of SnO_2 and SnO_2–rGO

Sample	Mean diameter D (nm)
SnO_2	11
SnO_2–rGO (2.5 : 1)	9
SnO_2–rGO (1.25 : 1)	5
SnO_2–rGO (1 : 1)	2.5

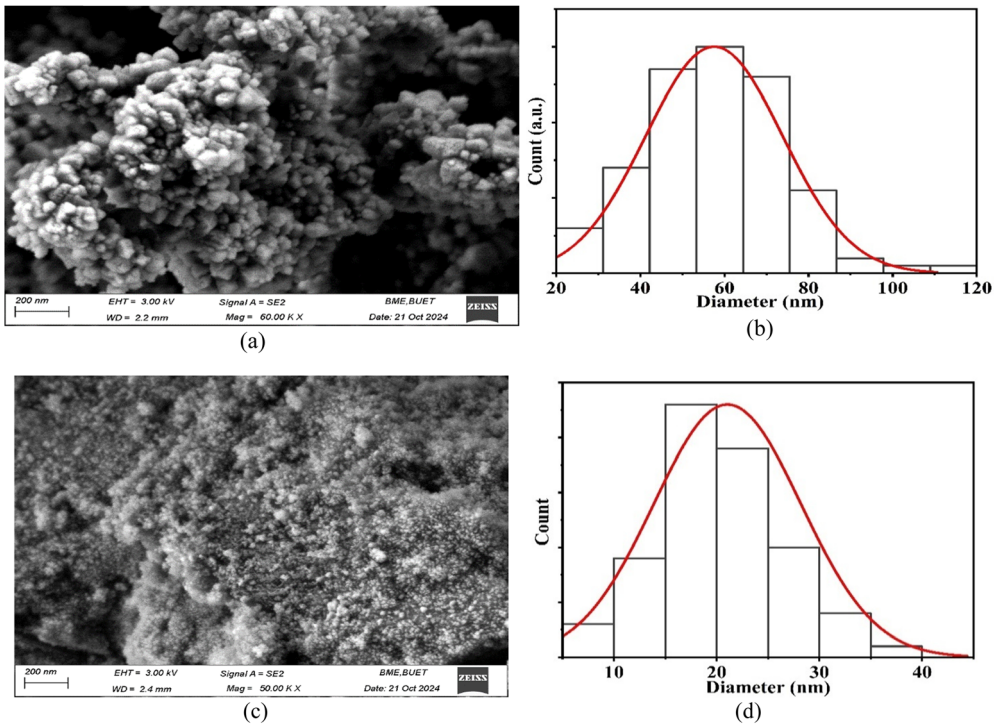

Fig. 5 (a) FESEM of SnO_2, (b) FESEM of SnO_2–rGO; (c) and (d) particle size distribution histograms of the SnO_2 and SnO_2–rGO nanocomposites.

SnO_2 nanoparticles are more uniformly distributed across the rGO sheets, which act as a scaffold to reduce agglomeration. The rGO sheets not only help to disperse the SnO_2 NPs but also play an active role in preventing the formation of large aggregates. This dispersion is essential for enhancing the material's surface area and enhancing the transport of charge carriers.[96]

3.4 Raman analysis

The Raman spectrum of SnO_2 is presented in Fig. 6(a) (left panel), in which a broad peak at 493 cm^{-1} is observed and convoluted into five constituent phonon mode frequencies at 279, 408, 460, 494, and 609 cm^{-1}. These are assigned as E_g, S_1, S_2, S_3, and A_{1g} where E_g and A_{1g} are Raman allowed modes for SnO_2 NPs. Whereas other frequency modes S_1, S_2, and S_3 appear due to the abundant existence of the in-plane oxygen vacancies in SnO_2 NPs.[97,98] Fig. 6(b) (right panel) presents the Raman spectra of SnO_2–rGO NCs, which have two prominent features at 1337 cm^{-1} and 1611 cm^{-1}, related to the D band and G band of graphene, respectively.[93,99] The disorder mode (D band) arises from the structural defect states and impurities of graphene, and the G band appears due to the in-phase vibration of the graphite lattice. The intensity ratio of the D and G bands (I_D/I_G ratio) helps to estimate the defects of graphene-based samples, where a higher ratio ensures more defects on

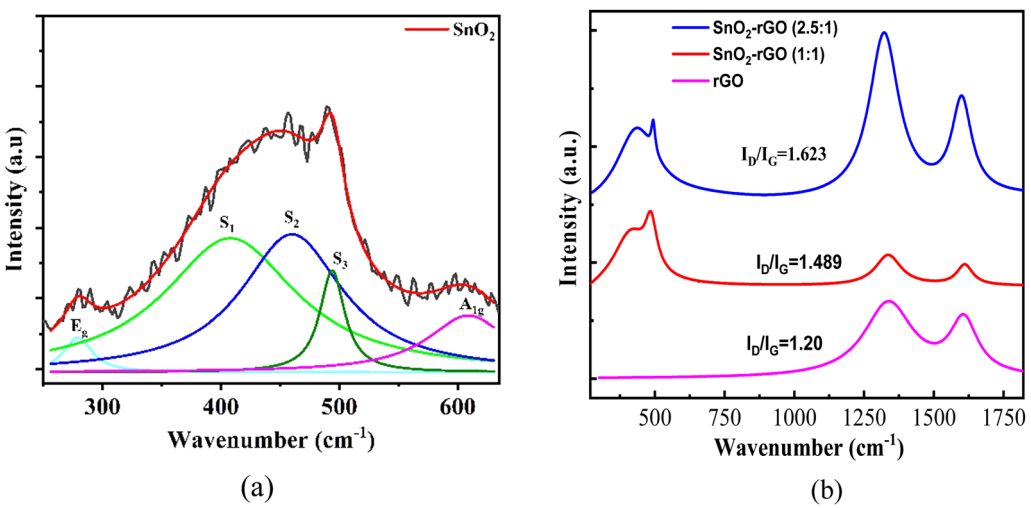

Fig. 6 (a) Raman spectra of the synthesized SnO_2, and (b) Raman spectra of the synthesized rGO, and SnO_2–rGO nanocomposites.

graphene. The intensity ratios (I_D/I_G) of peak D to peak G of rGO and SnO_2–rGO NCs are 1.20, 1.489, and 1.623, respectively. The degree of peak intensity ratio (I_D/I_G) for SnO_2–rGO NCs are higher than rGO, which suggests the reduction in the sp^2 carbon domain and presence of a greater number of defects caused by the growth of grain boundaries, oxygen-vacancies, amorphous carbon species, and the attachment of SnO_2 nanoparticles on the rGO sheet.[100] However, in the NC material, the D band and G band experience a small blueshift and appear at 1321 cm^{-1} and 1598 cm^{-1}. These shifts indicate strong interlayer coupling between SnO_2 and rGO. This defect plays an important role in inducing a charge transfer mechanism.

3.5 FTIR and PL analysis

Fourier transform infrared (FTIR) spectroscopy (Fig. 7) was used to investigate the chemical interactions and functional groups within the SnO_2–rGO NCs. The characteristic peak of SnO_2 at 660 cm^{-1} was split into peaks at 630 cm^{-1} and 690 cm^{-1} for the SnO_2–rGO NCs after adding GO to the SnO_2 matrix, confirming the formation of nanocomposites and the structural integrity of the SnO_2 lattice within the nanocomposites.[101,102] The presence of this peak across all samples demonstrates that the primary SnO_2 structure is retained, even with the incorporation of GO (later turned into rGO). Notably, as the rGO content in the composite increases, the 660 cm^{-1} absorption peak broadens and decreases in intensity. This broadening and decrease in intensity suggest that there are strong interactions between the SnO_2 nanoparticles and the rGO matrix. These interactions likely indicate the formation of robust chemical bonds between SnO_2 and rGO, possibly involving covalent Sn–O–C linkages. The FTIR spectra also reveal the absence or weakening of characteristic GO peaks, such as those for C═O (around 1725 cm^{-1}) and C═C stretching vibrations (around 1600 cm^{-1}). The IR peaks corresponding to 2933 cm^{-1} and 2852 cm^{-1} are due to the asymmetric and symmetric CH_2 stretching of GO, respectively. These changes suggest that partial reduction of GO occurs during the composite synthesis process. The reduction of GO, which is typically accompanied by the removal of

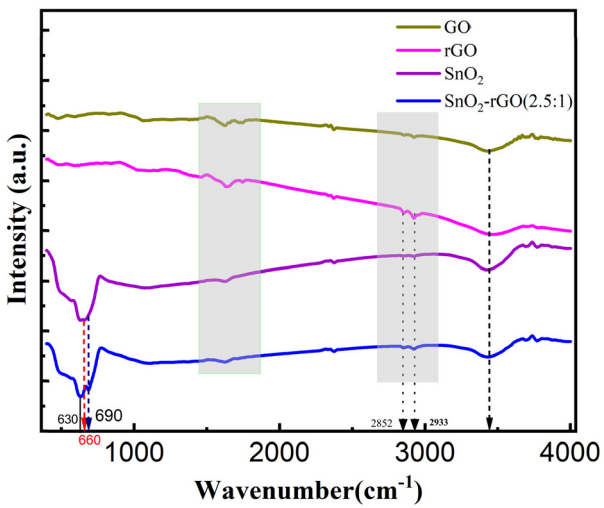

(a)

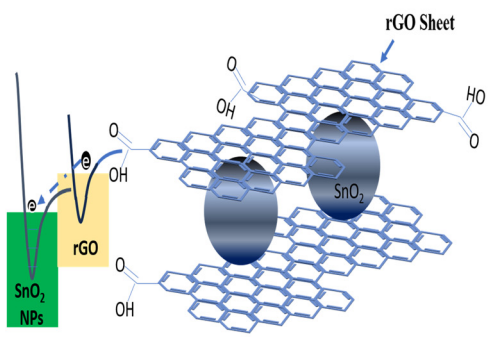

(b)

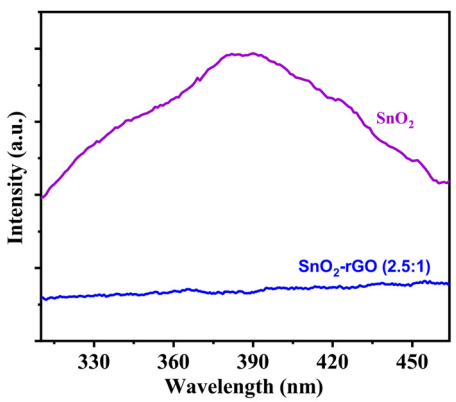

(c)

Fig. 7 Study of the surface functionalization of SnO_2, GO, rGO, and SnO_2–rGO nanocomposites through FTIR spectroscopy. *(c) PL spectra of SnO_2* and SnO_2–*rGO (2.5 : 1)*.

oxygen-containing functional groups, leads to an increase in its electronic conductivity and facilitates better charge transport within the composite.[101,103]

Photoluminescence (PL) measurements were carried out on SnO_2 and SnO_2–rGO nanocomposites to investigate the charge transfer mechanism, as illustrated in Fig. 3(c). The data indicate that pristine SnO_2 exhibits strong photoluminescence, characterized by a broad emission peak centered around 380 nm. On the other hand, no significant PL peak has been found in SnO_2–rGO and its spectrum is flatter than that of SnO_2. Remarkably, the PL intensity becomes significantly quenched and a significantly flat spectrum in SnO_2–rGO (2.5 : 1) is exhibited in comparison with SnO_2, demonstrating a prominent charge transfer.[92,97] The formation of covalent bonds within the hybrid structure alters the electronic characteristics of both rGO and SnO_2, resulting in the quenching and a spectral shift of the PL emission peak. Since rGO has no bandgap and conducts electricity very well, it easily attracts the excited electrons from SnO_2's conduction band through its π-conjugated structure. This suggests that the addition of rGO suppresses electron–hole recombination, resulting in the observed quenching effect. Moreover, the extent of recombination is influenced by the conjugation length of the carbon bonds and the size of the sp^2 domains.[92]

3.6 Nonlinear optical properties

Fig. 8(a)–(c) and 9(a)–(c) display the CA Z-scan experimental data (shown by the circles) with theoretical fitting (shown by the red solid lines for SBF and dashed black lines for TLM), for three batches of pure GO samples with three different concentrations at two input peak intensities 1.0 kW cm^{-2} and 5.3 kW cm^{-2} respectively. The variations of peak–valley difference (ΔT_{p-v}) of pure GO by changing its concentrations are also shown in Fig. 8(d) and 9(d) and it is observed that the peak–valley difference (ΔT_{p-v}) increases monotonically with the increment of the concentrations of the pure GO in both cases. But at very low input peak intensity (1.0 kW cm^{-2}), CA Z-scan curves of pure GO exhibit asymmetry and this asymmetric behavior comes due to the contribution of nonlinear absorption, high nonlinear phase shift and the nonlocal thermal nonlinear refraction.[66–70,72,104,105] The nonlinear absorption (NLA) mechanism in samples may be invoked by various NLO processes like two-photon absorption (TPA), excited state absorption (ESA), free carrier absorption (FCA), and reverse saturable absorption (RSA).[54] The Sheik-Bahae formalism (SBF)[64] and thermal lens model (TLM)[71] have been used as theoretical models to perform the fitting processes. It is observed that in Fig. 8(a)–(c), the thermal lens model (TLM) has a better fit than

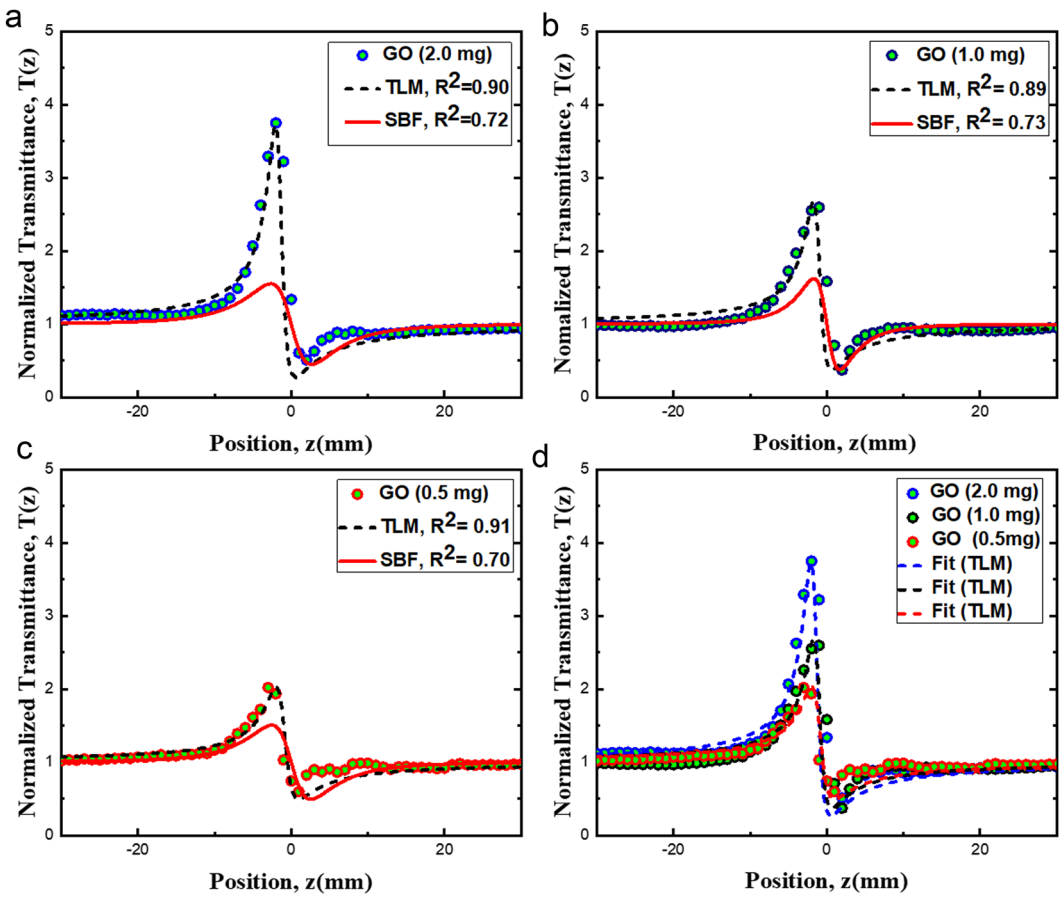

Fig. 8 CA Z-scan experimental data with the theoretical fit of GO nano-composites (a) GO (2.0 mg ml^{-1}), (b) GO (1.0 mg ml^{-1}), and (c) GO (0.5 mg ml^{-1}), respectively, at a peak intensity of I_0 = 1.00 kW cm^{-2}. (d) Peak–valley difference in a single plot.

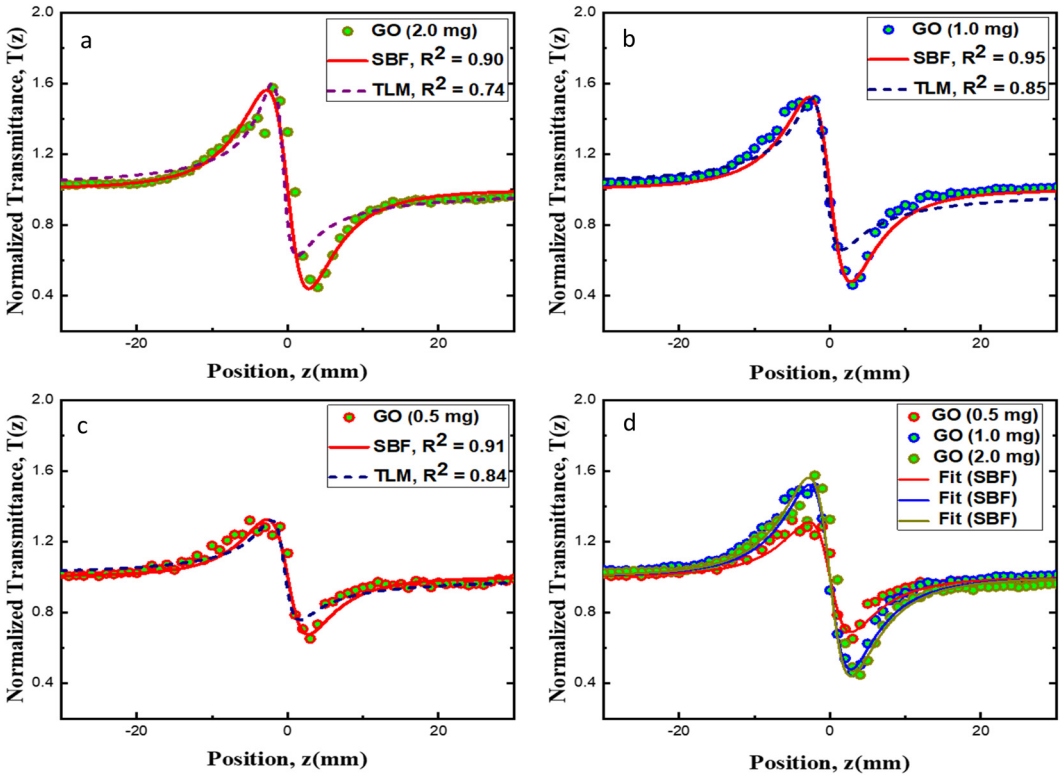

Fig. 9 CA Z-scan experimental data with the theoretical fit of GO (a) GO (2.0 mg ml^{-1}), (b) GO (1.0 mg ml^{-1}), and (c) GO (0.5 mg ml^{-1}), respectively, at a peak intensity of I_0 = 5.3 kW cm^{-2}. (d) Peak–valley difference in a single plot.

the conventional Sheik-Bahae formalism (SBF). All pure GO samples showing a peak–valley separation greater than $1.7z_0$ (around $3z_0$) is a clear indication of thermal nonlinearity.[65,71,106] This theoretical fitting confirms that at very low intensity of a CW laser the thermal lensing effect is the major mechanism that leads to the nonlinear absorption with a self-defocusing effect. The normalized transmittance curve shows a maximum asymmetric peak followed by a minimum valley at a higher concentration of GO because these thermal effects due to CW laser excitation may induce the ESA, *TPA, and RSA or SA* process in the material.[80,106–109] For pure GO, the enhancement of nonlinear refractive index (the peak to valley difference increases) with the increment of the concentrations of pure GO can be attributed to several nonlinear optical mechanisms such as the electrostrictive effect, molecular reorientation, electronic polarization, excited state refraction, and thermal lensing.[68,71,105] Conversely, when the input peak intensity is increased to 5.3 kW cm^{-2}, the CA measurements for each GO batch display a symmetric peak-to-valley curve. This symmetry suggests that the nonlinear refractive index n_2 is negative, and that nonlinear absorption has a negligible impact on shaping the curve. The symmetric behavior of the curves shows that at relatively higher input peak intensity, the nonlinear scattering, nonlinear refraction becomes dominant. It is noted that the shape of the obtained experimental CA Z-scan curve in Fig. 9(a)–(c), 11(a)–(c), 12(a)–(c) and 13(a)–(c) is better described by the SBF than the TLM. The reason may be that, in addition to the thermal lensing effect, other mechanisms that could be responsible for the observed nonlinearity include electrostriction, molecule reorientation, local field enhancement, and the Soret effect. Compared to TLM, the local SBF model would offer a more accurate description in this situation. Furthermore, since the thermal diffusion coefficient of graphene is very high, the contributions of cumulative thermal effects in graphene are negligible. In liquid media (*i.e.*, when dispersed in solution), nonlinear refraction under CW or long-pulse laser excitation arises from the behavior of π electrons, as well as the reorientation and alignment of graphene sheets. In the case of GO dispersions, contributions to nonlinear refraction come not only from π electrons but also from the electrons in sp^2 and sp^3 hybridized domains, along with free carriers. Measured values of the nonlinear phase shift and nonlinear refractive index of all samples are given in Table 2.

It is noted that a small Z-scan signal has only been detected for 2.0 mg of SnO_2, as shown in Fig. 10. But no close-aperture Z-scan signal has been detected for pure SnO_2 at the two specific concentrations of 0.5 mg and 1.0 mg. On the other hand, it is observed that both GO and rGO have better nonlinearity than SnO_2. We anticipated that by mixing pure SnO_2 with varying ratios in GO, the nonlinearity of pure SnO_2 could be tuned since pure GO had sufficient nonlinearity.

Fig. 11(a)–(c), 12(a)–(c), and 13(a)–(c) display the CA Z-scan experimental data (shown by the circles) with theoretical fitting (shown by the red solid lines for SBF and dashed black lines for TLM), for three batches of samples with three different concentrations for three different ratios of SnO_2 : GO 1 : 1, 1.25 : 1 and 2.5 : 1 respectively.

Table 2 Measured values of the nonlinear phase shift and nonlinear refractive index of pure SnO_2, RGO, GO, and SnO_2–rGO nano-composites with varying the amount of SnO_2

Samples	Linear absorption coefficient at an excitation wavelength of 532 nm, α (mm^{-1})	Nonlinear phase shift from SBF fit, $\lvert\Delta\phi_0\rvert$ (rad) at peak intensity I_0 = 5.3 kW cm^{-2}	Nonlinear phase shift from TLM fit, $\lvert\Delta\theta\rvert$ (rad) at peak intensity I_0 = 5.3 kW cm^{-2}	Nonlinear refractive index, n_2 (10^{-8} W cm^{-2})	Nonlinear refractive index, n_2^{th} (10^{-9} W cm^{-2})
SnO_2 (2.0 mg ml^{-1})	0.177331	1.09335 ± 0.05869	0.17964 ± 0.00806	1.90613 ± 0.102319	3.13182 ± 0.140517
rGO (2.0 mg ml^{-1})	0.80467	1.61501 ± 0.02401	0.29052 ± 0.04320	3.75600 ± 0.055837	6.76000 ± 0.10000
GO (0.5 mg ml^{-1})	0.43757	1.60083 ± 0.05763	0.28049 ± 0.023401	3.15761 ± 0.113674	5.53262 ± 0.461581
GO (1.0 mg ml^{-1})	0.502054	2.56998 ± 0.06840	0.42061 ± 0.02307	5.2222 ± 0.138989	8.5468 ± 0.468783
GO (2.0 mg ml^{-1})	0.748475	2.76865 ± 0.04640	0.47519 ± 0.01430	6.28294 ± 0.105296	10.7836 ± 0.324512
Nano-composite, NC1 [SnO_2–rGO (1 : 1)]					
NC1 (0.5 mg ml^{-1})	0.3910	0.9408 ± 0.012701	0.14164 ± 0.00971	1.81591 ± 0.0245152	2.73391 ± 0.18742
NC1 (1.0 mg ml^{-1})	0.4508	1.51418 ± 0.03545	0.27372 ± 0.01511	3.00505 ± 0.0703543	5.43227 ± 0.299874
NC1 (2.0 mg ml^{-1})	1.0212	2.08303 ± 0.02310	0.3689 ± 0.012870	5.3112 ± 0.0588991	9.40601 ± 0.328152
Nano-composite, NC2 [SnO_2–rGO (1.25 : 1)]					
NC2 (0.5 mg ml^{-1})	0.4514	1.00108 ± 0.016702	0.16278 ± 0.01127	1.9873 ± 0.0331561	3.23144 ± 0.223727
NC2 (1.0 mg ml^{-1})	0.3984	1.53896 ± 0.027401	0.27538 ± 0.01542	2.98076 ± 0.053072	5.33373 ± 0.298664
NC2 (2.0 mg ml^{-1})	1.0179	2.47284 ± 0.021076	0.39583 ± 0.02245	6.29646 ± 0.0536647	10.0788 ± 0.571632
Nano-composite, NC3 [SnO_2–rGO (2.5 : 1)]					
NC3 (0.5 mg ml^{-1})	0.315511	1.10569 ± 0.01431	0.19035 ± 0.01021	2.05969 ± 0.0266568	3.54586 ± 0.190193
NC3 (1.0 mg ml^{-1})	0.603386	1.82533 ± 0.02364	0.32284 ± 0.01743	3.88376 ± 0.0502989	6.86908 ± 0.370859
NC3 (2.0 mg ml^{-1})	1.204469	3.06105 ± 0.01234	0.48306 ± 0.02292	8.41263 ± 0.0339138	13.2758 ± 0.629906

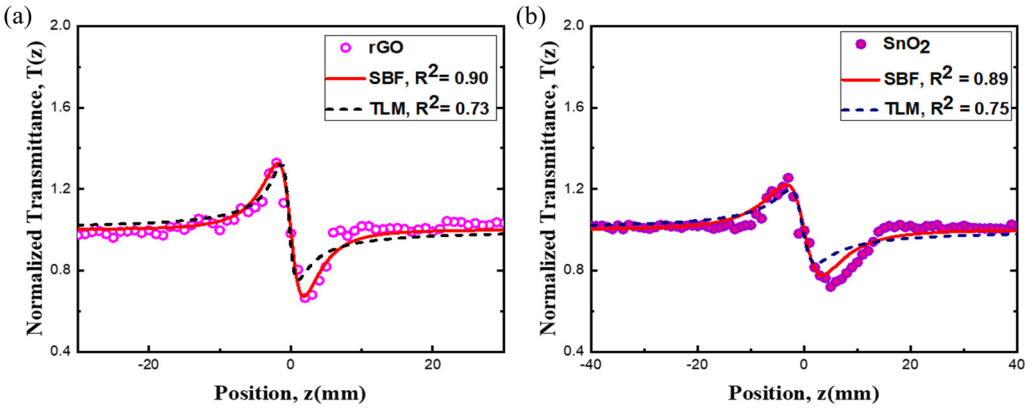

Fig. 10 CA Z-scan experimental data with the theoretical fit of (a) rGO (2.0 mg ml^{-1}) and (b) SnO_2 (2.0 mg ml^{-1}) at a peak intensity of I_0 = 5.3 kW cm^{-2}.

It is observed from the CA Z-scan curve that the peak–valley differences (ΔT_{p-v}) for each of the three nanocomposite ratios of SnO_2–rGO mixtures increase with the increment of their concentrations. The normalized transmittance curve shows a maximum peak followed by a minimum valley at higher concentrations (2 mg ml^{-1}) of all samples. For higher concentrations of each of the three batches of pure GO and different ratios of SnO_2–rGO, the enhancement of the nonlinear refractive index is found to be more significant. These can be attributed to the thermal lensing effect due to the temperature gradient in concentrated samples and enhancement of thermal conductivity, molecular reorientations, acoustic wave propagation due to thermal effect, or the electrostriction process in the continuous wave regime.[68,71,105] For high repetition rates, the sample does not have enough time to release the heat from the previous pulse out of the beam diameter because the interval between pulses is shorter than the characteristic time t_c which depends on the thermal diffusivity, thermal conductivity, material mass density and specific heat capacity at constant pressure.[110] Furthermore, it has been noticed that for a dilute pure SnO_2, the nonlinear signatures are negligible, as we have no CA Z-scan signals in our experiment. This may be due to the smaller concentrations of pure SnO_2 for which the thermal lensing effect is negligible.[105,107] As GO shows much better nonlinearity, it is possible to modulate the nonlinearity of both pure SnO_2 and GO by mixing them in different mass ratios. The reason for this better nonlinearity of GO may be attributed to the population redistribution of π electrons and the free carriers of the sp^2 domain.[55,111] Thermal lensing due to the local field effect also enhances the nonlinearity in GO.[54] From Fig. 14, it is observed that for certain higher concentrations (2 mg ml^{-1}), with the increment of GO in SnO_2, the nonlinearity of SnO_2–rGO significantly increased. This means that the pure GO enhances the nonlinearity in SnO_2–rGO nanocomposite samples, though SnO_2 has small nonlinear refraction rather than a nonlinear absorption optical signature.[112–114] From Fig. 14, one can see that with increasing the amount of SnO_2 in rGO sheets, the peak–valley difference (ΔT_{p-v}) (*i.e.* nonlinear

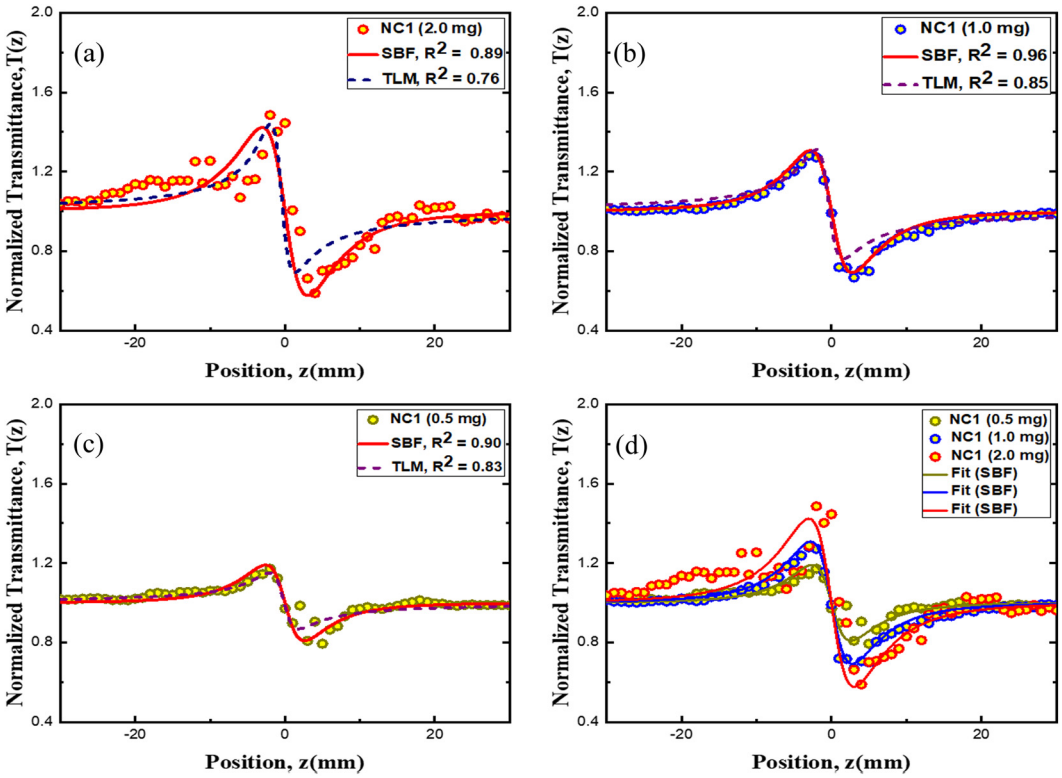

Fig. 11 CA Z-scan experimental data with the theoretical fit of NC1 [SnO_2–rGO (1 : 1)] nanocomposites (a) NC1 (2.0 mg ml^{-1}), (b) NC1 (1.0 mg ml^{-1}) and (c) NC1 (0.5 mg ml^{-1}) respectively at a peak intensity of I_0 = 5.3 kW cm^{-2}. (d) Peak–valley difference in a single plot.

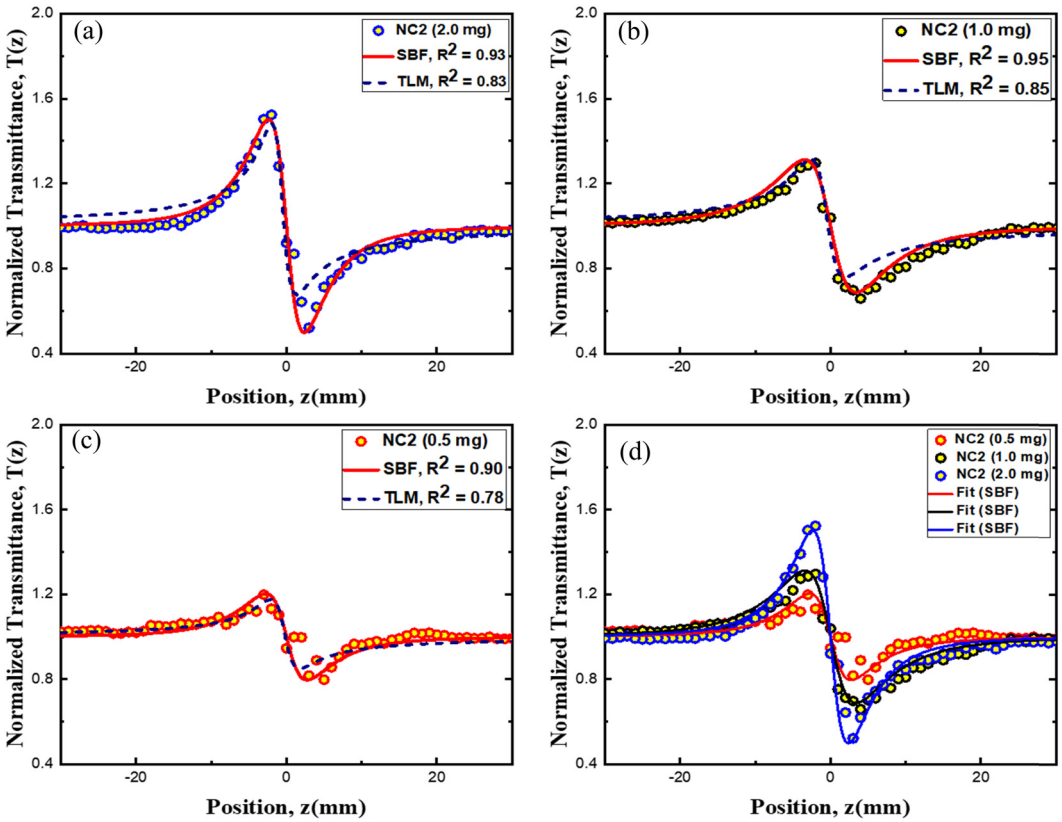

Fig. 12 CA Z-scan experimental data with the theoretical fit of NC2 [SnO_2–rGO (1.25 : 1)] nanocomposites (a) NC2 (2.0 mg ml^{-1}), (b) NC2 (1.0 mg ml^{-1}) and (c) NC2 (0.5 mg ml^{-1}), respectively, at a peak intensity of I_0 = 5.3 kW cm^{-2}. (d) Peak–valley difference in a single plot.

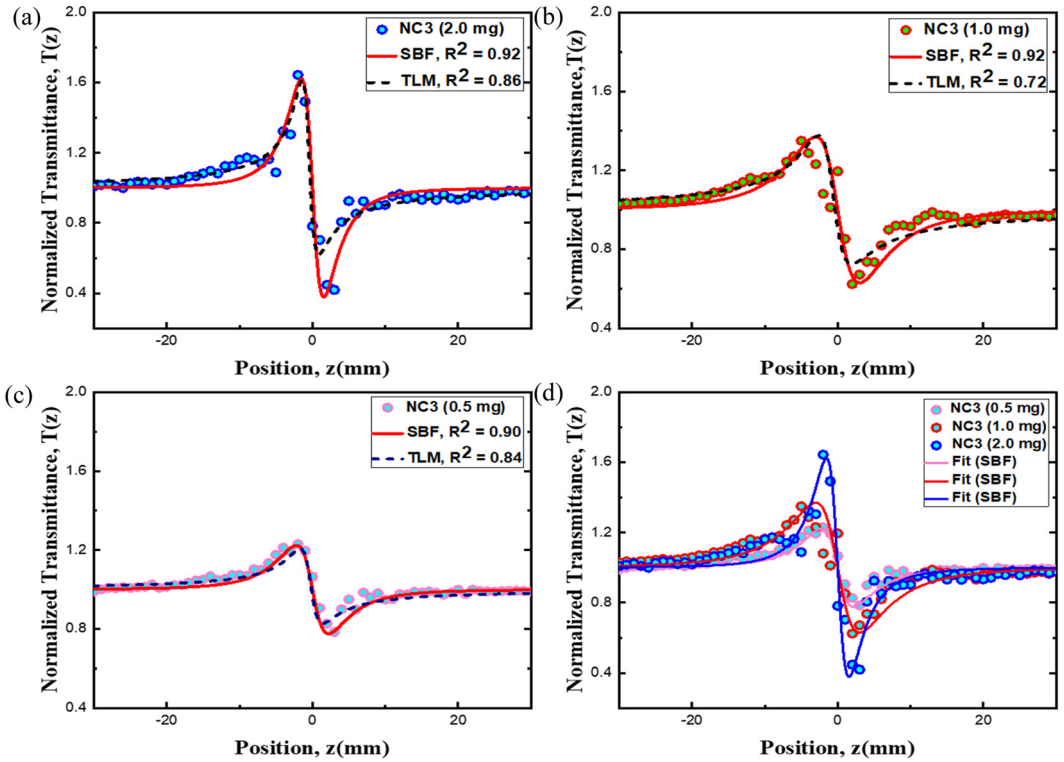

Fig. 13 CA Z-scan experimental data with the theoretical fit of NC3 [SnO_2–rGO (2.5 : 1)] nanocomposites (a) NC3 (2.0 mg ml^{-1}), (b) NC3 (1.0 mg ml^{-1}) and (c) NC3 (0.5 mg ml^{-1}), respectively, at a peak intensity of I_0 = 5.3 kW cm^{-2}. (d) Peak–valley difference in a single plot.

phase shift, $\Delta\phi_0$) also increases. Three nanocomposite ratios 1 : 1, 1.25 : 1, and 2.5 : 1 of the SnO_2–rGO mixture show better nonlinearity than pure SnO_2, and this means one can tune the nonlinearity of SnO_2 by its amount in GO with different ratios. Moreover, it is very interesting to see that SnO_2–rGO (2.5 : 1) of the same concentrations (2 mg ml^{-1}) shows better nonlinearity than pure GO and rGO itself. Moreover, the theoretical fitting of the symmetric Z-scan CA curve for the case of SnO_2–rGO nanocomposite samples, suggested that along the z-direction, the peak to valley separation, Δz_{p-v}, is about $1.7z_0$, indicating the contribution of electronic third-order nonlinearity.[65,106] That means the thermal lensing effect due to the local field effect in nanocomposites can play a minor role here. We believe that this improvement of the third-order nonlinear refractive index for SnO_2–rGO nanocomposite samples originates from other different origins, such as exciton oscillator strength, local field enhancement, molecular reorientations, electrostriction effect, charge transfer mechanism, excited state refraction, free carrier refraction, and defect states. Furthermore, the localized surface plasmon resonance (LSPR), interband transitions, free charge carrier density, and large metal nonlinear response may also improve the nonlinear properties of nanocomposites. Among all of these, the charge-transfer across the interface of the SnO_2–rGO composite and induced defect states can play the dominant role for this drastic enhancement of nonlinear refractive index n_2 for these nanocomposites.[16,111,115,116] The synergistic effect due to charge transfer characteristics of SnO_2–rGO nanocomposite materials may play a crucial role in enhancing the nonlinear properties. The charge-transfer mechanism occurs in SnO_2–rGO nanocomposites due to their work function mismatch.[97] In this mechanism, rGO was regarded as the electron donor and SnO_2 as the electron acceptor. With the increase in the amount of SnO_2 in SnO_2–rGO nano composites, the possibility of forming an electron donor–acceptor pair between SnO_2 and rGO increased, and more charges were transferred through the interface. This charge transfer process and the synergistic effect of the composites are responsible for this significant enhancement of the nonlinear optical properties of SnO_2–rGO. Our PL and Raman spectroscopic analysis confirmed that the charge-transfer mechanism played a more significant role in SnO_2–rGO (2.5 : 1) nanocomposites due to its higher defects. We believe that in SnO_2–rGO (2.5 : 1) nanocomposites the charge-transfer mechanism and defect states might play major roles and for this reason it exhibits better nonlinearity than rGO itself and other samples SnO_2–rGO (1.25 : 1) and SnO_2–rGO (1 : 1). Moreover, the concentration of exciton oscillator strength and the local electric field enhancement existing at the interface between rGO and SnO_2 grains may also increase the third-order nonlinearity in the SnO_2–rGO nano composite.[54,117,118] Additionally, the value of n_2 is impacted by the photo-induced redistribution of the effective local electric field on the interface of SnO_2–rGO nano-composites, causing the thermal lensing effect, which may be altered by an increase in SnO_2 nanoparticle content.[54,119]

However, we have already mentioned that at lower intensity (1.0 kW cm^{-2}) all Z-scan curves show (Fig. 8) asymmetry due to

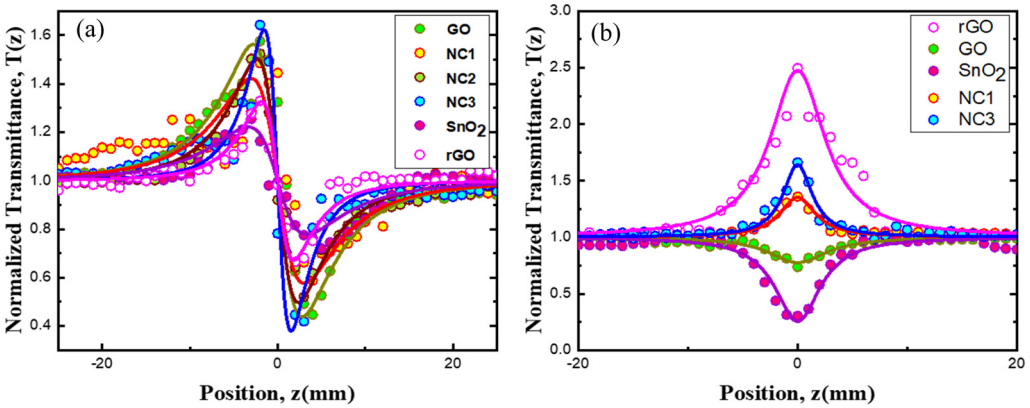

Fig. 14 (a) Normalized close-aperture (CA) data with theoretical fitting in a single plot for pure SnO_2, GO, rGO, NC1, NC2, and NC3 nanocomposites with different mass ratios of maximum concentrations (2.0 mg ml^{-1}) at I_0 = 5.3 kW cm^{-2}. (b) Normalized open-aperture (OA) data with theoretical fitting in a single plot for pure SnO_2, GO, rGO, NC1, and NC3 of two different ratios at I_0 = 1.00 kW cm^{-2}.

the contribution of nonlinear absorption (β) and for this reason, it has been expected that there should be a significant open aperture signal. It should also be noted that at the input peak intensity (I_0 = 5.3 kW cm^{-2}) all Z-scan measurements present a negligible open aperture signal due to the totally refractive effect, as it is not affected by absorption saturation or excited state absorption.[80] But at relatively lower intensity, the concentrations of the samples play an important role, and at higher concentrations (2 mg ml^{-1}), show significant open aperture signals. It is noted that at lower concentrations, it does not show any significant OA signal. Fig. 14(b) exhibits the typical open-aperture (OA) Z-scan curves at lower intensity (I_0 = 1.0 kW cm^{-2}) with theoretical fitting for the pure SnO_2, pure GO, pure rGO and SnO_2–rGO nanocomposites with mass ratios of (1 : 1) and (2.5 : 1) at the wavelength of 532 nm. The nonlinear absorption coefficient and parameters of all the samples extracted from theoretical OA fittings are given in Table 3.

The OA traces for pure GO and SnO_2 show a symmetric valley shape curve ($0 < \beta$) about $z = 0$, which indicates that the physical origins are reverse saturation absorption (RSA). The wider band gap ($E_{laser} < E_g$) of SnO_2 and the relatively higher band gap of sp^3 domains in GO[39] ($E_{laser} < E_g$) suggest that the two-photon absorption (TPA) and excited state absorption (ESA) is a possible mechanism for RSA. At lower intensities of a continuous-wave (CW) laser, thermal effects become more significant. Additionally, as the energy band gap (E_g) decreases, the likelihood of TPA further reduces. When the samples are exposed to CW laser light, localized heating occurs, which can lead to more thermally driven excited-state absorption (ESA) than TPA.[54,120,121] Theoretical fit using eqn (4b) also suggests that the underlying RSA mechanism arises due to ESA and TPA. From Fig. 14b, it is seen that the depth of the valley of the OA symmetric curve for pure SnO_2 is greater than pure GO, and it suggests that pure SnO_2 has greater ESA and TPA cross-sections than pure GO. But in the case of rGO and SnO_2–rGO nanocomposites, there is a flip in the edges of the nonlinear absorption OA curve (showing a peak at the focus, *i.e.*, $0 > \beta$), indicating the presence of saturation absorption (SA). The normalized OA curve of rGO showed a large peak at focus, indicating that rGO has a strong saturation absorption (SA) character at this intensity, attributable to the strong Pauli blocking effects due to its unique lower band-gap structure similar to graphene.[39,122,123] In SnO_2–rGO nanocomposites, the transition from RSA to SA is a consequence of competition between the TPA of SnO_2 and SA of rGO.[124] The two major possible physical reasons for the tuning behavior of the SA effect in SnO_2–rGO nanocomposites can be attributed to the efficient charge transfer from rGO to SnO_2 in the SnO_2–rGO nanocomposite and localized defects in the nanocomposites. Moreover, for different mass ratios of nanocomposites, the large number of induced defect states also plays a crucial role.[125] Raman and PL spectra confirmed the charge transfer mechanism and existing defects in SnO_2–rGO nanocomposites. We also perform the intensity-dependent OA Z-scan experiment for all the samples which are included in the SI. At lower concentrations, none of the samples show any observable OA data. At higher concentrations (2 mg ml^{-1}), all

Table 3 Measured values of the nonlinear absorption coefficient and parameters of pure SnO_2, pure GO, and SnO_2–rGO nano-composites

Samples	Linear absorption coefficient at an excitation wavelength of 532 nm, α (mm^{-1})	Nonlinear absorption coefficient, β (10^{-3} cm W^{-1})	Imaginary part of susceptibility, $Im(\chi^{(3)})$ (10^{-7} esu)	FOM (10^{-8} esu cm)	Saturation intensity, I_{sat} (kW cm^{-2})
SnO_2	0.177331	6.580 ± 0.01580	24.9385 ± 0.0599	140.632	1.54 ± 0.020
GO	0.748475	0.812 ± 0.00340	3.0775 ± 0.0129	4.112	4.60 ± 0.018
rGO	0.80467	−(12.821 ± 0.825)	48.5922 ± 3.1268	60.388	28.64 ± 0.103
NC1	1.0212	−(0.8070 ± 0.0070)	3.0586 ± 0.0265	2.995	12.97 ± 0.400
NC3	1.204469	−(5.00833 ± 0.0467)	18.9818 ± 0.177	15.759	22.80 ± 0.309

samples show significant OA signals. For pure SnO_2 and GO, it is noted that with the increase in the input intensities, the values of β decrease. At lower intensities of 1000 W cm^{-2} and 3000 W cm^{-2}, both SnO_2 and GO exhibit significant symmetric OA Z-scan signals due to RSA effects. This dominating RSA effect originates from ESA and TPA. At a higher intensity of 5300 W cm^{-2}, they showed very small NA effects rather than exhibiting asymmetric CA data due to the pre-dominating nonlinear refraction, scattering, and lensing effects. On the other hand, both rGO and SnO_2–rGO nanocomposites show a dominating SA effect. It is noted that ESA leads to both SA and RSA.[126,127] When the absorption cross-section of the excited state is lower than that of the ground state, the transmittance OA curve exhibits a symmetric peak at the focus, which is known as SA. For rGO and rGO-based nanocomposite materials with defect density, the filling of the localized defect states leads to SA behavior with the increase or decrease in the input intensity. At lower pump intensities, the SA shown by rGO and SnO_2–rGO nanocomposites is probably due to the state-filling effect of the interband transition in the sp^2 domains.[126] It is observed that rGO has a better SA effect than SnO_2–rGO nanocomposites. The intensity-dependent tunable SA behavior of our SnO_2–rGO can be attributed to the presence of a large number of defect states. We explain it using a schematic energy diagram for the proposed NA and SA mechanisms in Fig. 15(a).[128,129] When 532 nm laser light (2.32 eV photon) is incident on the samples, the one-photon absorption (OPA) from the valence band was sufficient to excite an electron from this state to the defect states of both the rGO sample and SnO_2–rGO nanocomposites. Some of these electrons could lose their energy and make transitions to the valence band. On the other hand, some of these electrons in defect states could be excited to the conduction band by the absorption of another photon.[130] Our Raman spectra confirm that SnO_2–rGO nanocomposites have more defects than rGO, and this is one of the major reasons that rGO exhibits a better SA effect than all SnO_2–rGO samples. The lower density of the defect states was filled by OPA, and the SA effect became dominant. Moreover, these defect sites behave as a center for exciting electron trapping, and control the photon-stimulated electron-hole pair recombination process.[131]

To gain further insights into the charge transfer mechanism and formation of defect states in the SnO_2–rGO nanocomposites, we performed density functional theory (DFT) calculations using VASP.[81–84] The DFT-optimized structure of the SnO_2–rGO heterostructure is displayed in Fig. 15. This structure, although

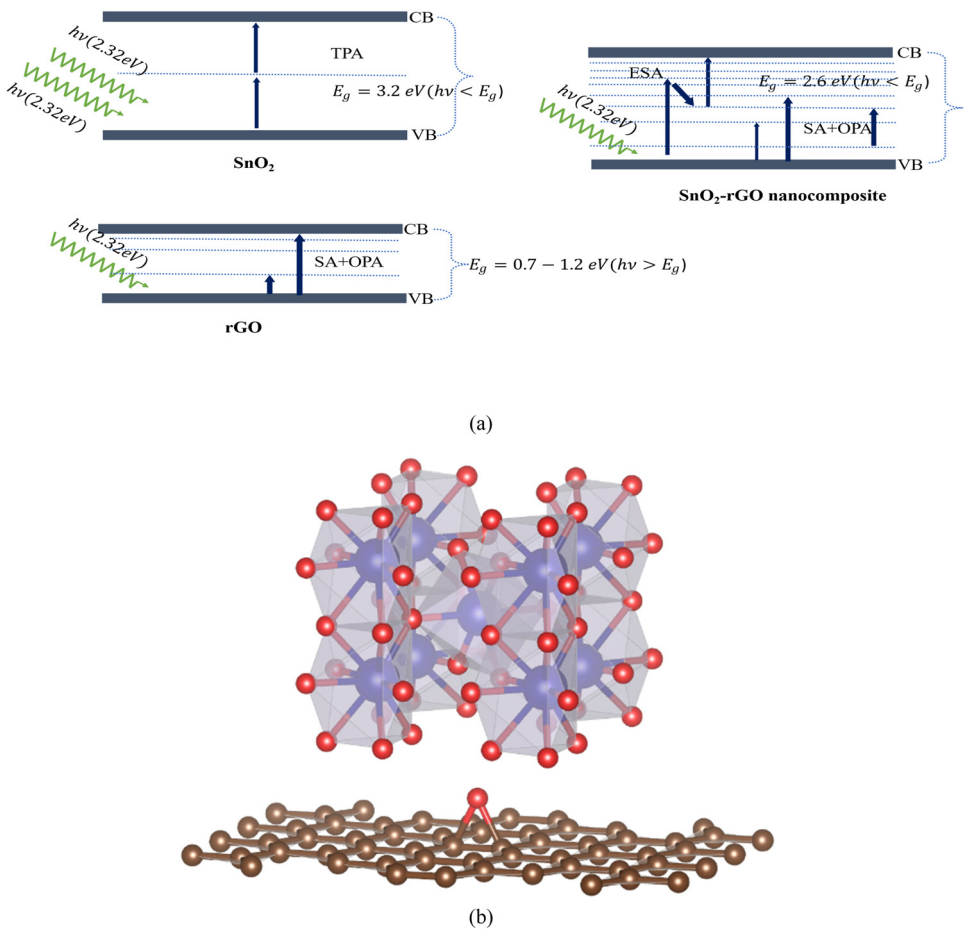

Fig. 15 (a) Schematic energy diagram for the NA and SA mechanisms, and (b) optimized structure of the SnO_2–rGO heterostructure. Red, brown, and blue colored atoms represent O, C, and Sn, respectively.

having a different size and morphology from the experimental system, can be exploited to explain the charge transfer mechanism. Furthermore, we plotted the partial density of states (PDOS) for the Sn 4d and C 2p orbitals of SnO_2, rGO, and SnO_2–rGO to account for orbital interactions and charge transfer phenomena. The PDOS plots as a function of energy (E–E_F), where the vertical dashed line represents the Fermi level energy, E_F, displayed in Fig. 16(a) and (b), provide insights into the distribution of electronic states within the Sn 4d orbital before and after the hybridization process, respectively. Similar representation has been done for the C 2p orbital in Fig. 16c and d. The Sn 4d orbital of SnO_2 exhibited an overall enhancement of states in the vicinity of the Fermi level after hybridization with rGO, as seen in Fig. 16a and b. In contrast, the C 2p orbital of rGO showed a reduction of states above the Fermi level ($\sim$2 eV–3 eV), as depicted in Fig. 16c and d. Therefore, we can conclude that charge is being transferred from rGO to SnO_2, which supports our experimental findings.

Moreover, the greater the extent of metal oxide, the higher the chance for electron transfer, which leads to enhanced NLO responses of the decorated nanocomposite samples and exhibits tunable saturable absorbers as well as optical limiting devices. The combined effects of localized field enhancement due to the surface plasmon resonance (SPR) effect, increased free charge carriers, and the quantum confinement effect can play important roles. Additionally, the concentrations of the samples can also affect their nonlinear absorption behavior.[132] At lower intensities, this higher concentration enables the SnO_2–rGO nanocomposite samples to possess a greater number of free electrons due to the defects, which in turn contributes to the enhanced SA. Additionally, at the corresponding wavelength in the CW regime, the absorbance of the nonlinear material leads to an increase in temperature and density of the samples due to the large thermal expansion, which can also result in limiting action.

To demonstrate the optical limiting behavior of our sample, we estimated the normalized transmittance as a function of the input pump intensity of the incident laser beam. Fig. 17 presents the plot of normalized transmittance *versus* input pump intensity of our device observed for a CW laser of wavelength 532 nm up to a peak intensity of 1.00 kW cm^{-2}. To evaluate the optical-limiting characteristics, it is essential to investigate the strength of optical limiting using the onset threshold F_{ON} (the input intensity at which the normalized transmittance begins to diverge from its initial value) and optical limiting threshold F_{OL} (the input intensity threshold where the normalized transmittance decreases to less than 50%). From Fig. 17, the estimated optical limiting threshold F_{OL} values of SnO_2 and GO are 0.62 kW cm^{-2} and 1.21 kW cm^{-2} respectively. On the other hand, the onset threshold F_{ON} values of SnO_2, GO, rGO, NC1 and NC3 are 0.13 kW cm^{-2}, 0.16 kW cm^{-2}, 0.034 kW cm^{-2}, 0.10 kW cm^{-2}, and 0.08 kW cm^{-2} respectively. The optical limiting threshold of SnO_2 is approximately half that of GO. Thus, it can be interpreted that SnO_2 has better optical limiting performance than GO, as it exhibits lower F_{ON} and F_{OL} values. Moreover, rGO and SnO_2–rGO exhibit better SA effects and tunable SA effects. This means the tunable characteristics of our nanocomposites can be a potential candidate as a saturable

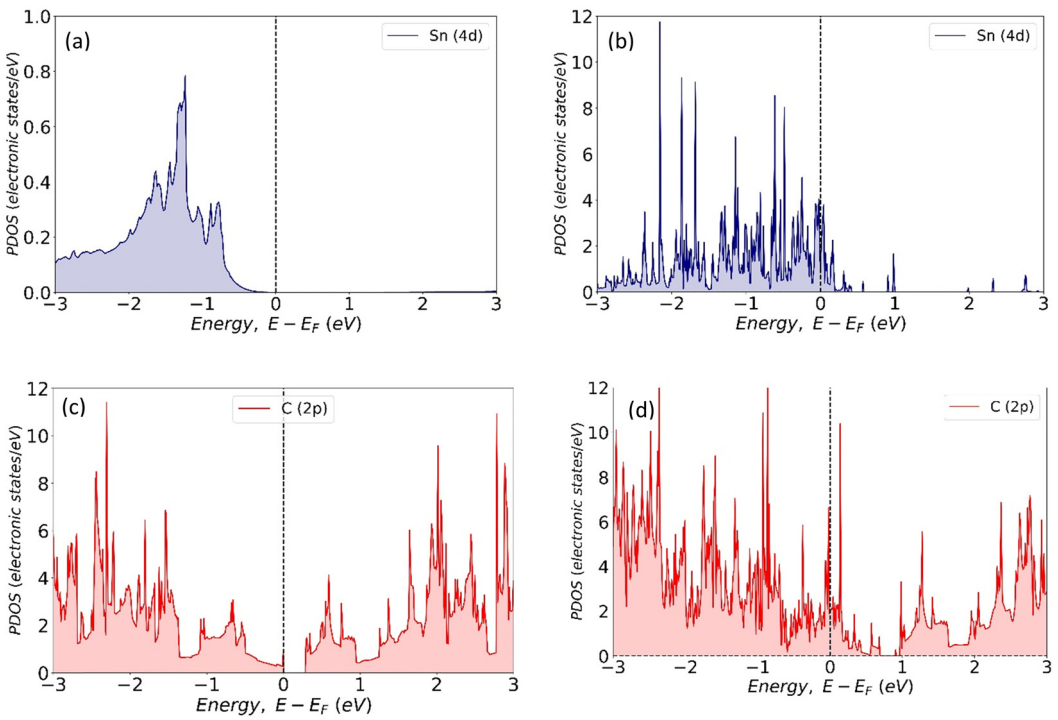

Fig. 16 PDOS plot for the Sn 4d orbital of SnO_2, (a) before and (b) after forming a heterostructure with rGO. PDOS plot for the C 2p orbital of rGO, (c) before and (d) after forming a heterostructure with SnO_2.

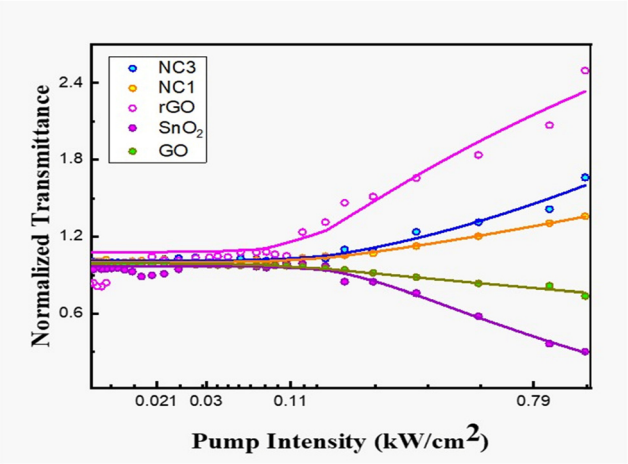

Fig. 17 Normalized transmittance as functions of pump intensity for SnO_2, GO, rGO, and SnO_2–rGO nanocomposites under an intensity of 1.00 kW cm^{-2} (532 nm).

absorber in mode-locking laser systems and optical logic gate devices.

Thus, this remarkable enhancement in the nonlinear refraction and nonlinear absorption (SA, TPA, RSA, ESA) of the nanomaterials and the saturable behaviour of SnO_2–rGO nanocomposites from RSA to SA suggests that it has the potential to be used as a tunable ideal optical device and other optical sensors. Our SnO_2–rGO nanocomposite can be used for developing photonics applications, optical data storage, controlling optical signals, and optical communications due to its self-defocusing behaviour and optical limiting switching behaviour.

4. Conclusion

In summary, we demonstrated a comparative study of the third-order nonlinearity of SnO_2–rGO nanocomposites using conventional Z-scan and thermal lensing models with a CW laser. Our results suggest that at lower intensity, the Z-scan curve shows asymmetry due to the contributions of nonlinear absorption and thermal effects. The thermal lensing effect due to the local field can play a major role here. Both SnO_2 and GO exhibit RSA that originates from thermal-induced ESA and TPA. On the other hand, SnO_2–rGO nanocomposites have a tuning SA character probably due to the charge transfer mechanism and induced defects. But at higher intensity, the symmetric Z-scan curve suggests that the contribution of nonlinear absorption is negligible. At this intensity, local SBF describes the Z-scan data better than the nonlocal TLM, indicating the minor contribution of thermal effects. The values of n_2 increase with the increment of the mass ratios of SnO_2–rGO nanocomposites, which exhibit self-defocusing effects. We believe that the synergistic effect due to the charge transfer characteristic of SnO_2–rGO nanocomposite materials and induced defects may play a crucial role in tuning the NLO properties. This study paves the way for the optimization of SnO_2–rGO nanocomposites for applications in optical limiters, mode-locking laser systems, switchers, and other nonlinear photonic devices, contributing to the development of more efficient materials in modern optics.

Conflicts of interest

The authors have no conflicts to disclose.

Data availability

Supplementary information is available. See DOI: **https://doi.org/10.1039/d5ma00790a**.

The datasets supporting this study are available from the corresponding author upon reasonable request. Any additional information required to reproduce the results can be provided by the authors upon request.

Acknowledgements

We extend our heartfelt thanks to the Department of Physics at the University of Dhaka for their support and collaboration. Our sincere appreciation also goes to the Centre for Advanced Research in Sciences (CARS), University of Dhaka, for providing the necessary experimental facilities. We are especially grateful to the Bangladesh University of Engineering and Technology (BUET) for their valuable resources and assistance. Lastly, we would like to express our deep gratitude to the Bangladesh Council of Scientific and Industrial Research (BCSIR) for granting us access to their experimental facilities, which played a vital role in this work. We would also like to thank the Bangladesh Research and Education Network (BDREN) for providing access to their server, which facilitated our computational study.

References

1 A. Redyuk, O. Sidelnikov and M. Fedoruk, *Opt. Commun.*, 2025, **578**, 131418.
2 C. Koos, L. Jacome, C. Poulton, J. Leuthold and W. Freude, *Opt. Express*, 2007, **15**, 5976–5990.
3 S. David, D. Chateau, H.-J. Chang, L. H. Karlsson, M. V. Bondar, C. Lopes, B. Le Guennic, D. Jacquemin, G. Berginc, O. Maury, S. Parola and C. Andraud, *J. Phys. Chem. C*, 2020, **124**, 24344–24350.
4 D. Hui, H. Alqattan, S. Zhang, V. Pervak, E. Chowdhury and M. T. Hassan, *Sci. Adv.*, 2023, **9**, eadf1015.
5 H. Wei, B. Li, W. Shi, X. Zhu, R. A. Norwood, N. Peyghambarian and S. Jian, *Sci. Rep.*, 2017, **7**, 1292.
6 L. Yan, Z. Gong, Q. He, D. Shen, A. Ge, Y. Dai, G. Ma, L. Sun and S. Zhang, *Nanophotonics*, 2024, **13**, 4429–4439.
7 M. He, C. Quan, C. He, Y. Huang, L. Zhu, Z. Yao, S. Zhang, J. Bai and X. Xu, *J. Phys. Chem. C*, 2017, **121**, 27147–27153.
8 O. Varnavski, C. Gunthardt, A. Rehman, G. D. Luker and T. I. I. I. Goodson, *J. Phys. Chem. Lett.*, 2022, **13**, 2772–2781.

9 K. Thambiratnam, N. Yusoff, S. N. Aidit, M. Z. Samion, N. A. Azali and H. Ahmad, *1D Semiconducting Hybrid Nanostructures*, John Wiley & Sons, Ltd, 2023, pp. 273–309.
10 G. Liu, H. Mu, F. Zhang, Y. Zeng, X. Bao, Z. Nie and Q. Bao, in *Fundamentals and Applications of Nonlinear Nanophotonics*, ed. N. C. Panoiu, Elsevier, 2024, pp. 393–440.
11 L. Sirleto and G. C. Righini, *Micromachines*, 2023, **14**(3), 604.
12 R. W. Boyd, *Nonlinear Optics*, Academic Press, San Diego, 3rd edn, 2008.
13 K. Wang, M. Seidel, K. Nagarajan, T. Chervy, C. Genet and T. Ebbesen, *Nat. Commun.*, 2021, **12**, 1486.
14 M. Lippitz, M. A. van Dijk and M. Orrit, *Nano Lett.*, 2005, **5**, 799–802.
15 A. Bhardwaj, N. M. Puthoor and G. G. Nair, *J. Phys. Chem. C*, 2020, **124**, 18698–18706.
16 M. Nadafan, M. Sabbaghan and Z. Ahmadi, *Diamond Relat. Mater.*, 2024, **146**, 111136.
17 H. Y. He, S. T. Pi, Z. Q. Bai, M. Banik, V. A. Apkarian and R. Q. Wu, *J. Phys. Chem. C*, 2016, **120**, 20914–20921.
18 N. J. J. Johnson, A. Korinek, C. Dong and F. C. J. M. van Veggel, *J. Am. Chem. Soc.*, 2012, **134**, 11068–11071.
19 D. Liu, J. Liu, K. Zhang, P. Wang, C. Miao, J. Sun, B. Zhang, J. He, X. Hao and Z. Yang, *J. Phys. Chem. C*, 2021, **125**, 803–811.
20 M. Kauranen and A. V. Zayats, *Nat. Photonics*, 2012, **6**, 737–748.
21 L. Wu, S. Patankar, T. Morimoto, N. L. Nair, E. Thewalt, A. Little, J. G. Analytis, J. E. Moore and J. Orenstein, *Nat. Phys.*, 2017, **13**, 350–355.
22 S. S. R. K. C. Yamijala, M. Mukhopadhyay and S. K. Pati, *J. Phys. Chem. C*, 2015, **119**, 12079–12087.
23 J. M. Hales, J. Matichak, S. Barlow, S. Ohira, K. Yesudas, J.-L. Brédas, J. W. Perry and S. R. Marder, *Science*, 2010, **327**, 1485–1488.
24 F. Giorgianni, E. Chiadroni, A. Rovere, M. Cestelli-Guidi, A. Perucchi, M. Bellaveglia, M. Castellano, D. Di Giovenale, G. Di Pirro, M. Ferrario, R. Pompili, C. Vaccarezza, F. Villa, A. Cianchi, A. Mostacci, M. Petrarca, M. Brahlek, N. Koirala, S. Oh and S. Lupi, *Nat. Commun.*, 2016, **7**, 11421.
25 F. Bonaccorso, Z. Sun, T. Hasan and A. C. Ferrari, *Nat. Photonics*, 2010, **4**, 611–622.
26 N. Liaros, P. Aloukos, A. Kolokithas-Ntoukas, A. Bakandritsos, T. Szabo, R. Zboril and S. Couris, *J. Phys. Chem. C*, 2013, **117**, 6842–6850.
27 A. Martinez and Z. Sun, *Nat. Photonics*, 2013, **7**, 842–845.
28 J. Wang, Y. Hernandez, M. Lotya, J. N. Coleman and W. J. Blau, *Adv. Mater.*, 2009, **21**, 2430–2435.
29 Z. Sun, A. Martinez and F. Wang, *Nat. Photonics*, 2016, **10**, 227–238.
30 K. F. Mak, M. Y. Sfeir, Y. Wu, C. H. Lui, J. A. Misewich and T. F. Heinz, *Phys. Rev. Lett.*, 2008, **101**, 196405.
31 M. Breusing, C. Ropers and T. Elsaesser, *Phys. Rev. Lett.*, 2009, **102**, 86809.
32 Z. Sun, T. Hasan, F. Torrisi, D. Popa, G. Privitera, F. Wang, F. Bonaccorso, D. M. Basko and A. C. Ferrari, *ACS Nano*, 2010, **4**, 803–810.
33 X.-L. Zhang, Z.-B. Liu, X.-C. Li, Q. Ma, X.-D. Chen, J.-G. Tian, Y.-F. Xu and Y.-S. Chen, *Opt. Express*, 2013, **21**, 7511–7520.
34 L. Liu, L. Wang, J. Gao, J. Zhao, X. Gao and Z. Chen, *Carbon*, 2012, **50**, 1690–1698.
35 G. Eda, Y.-Y. Lin, C. Mattevi, H. Yamaguchi, H.-A. Chen, I.-S. Chen, C.-W. Chen and M. Chhowalla, *Adv. Mater.*, 2010, **22**, 505–509.
36 Y. Zhang, T.-T. Tang, C. Girit, Z. Hao, M. C. Martin, A. Zettl, M. F. Crommie, Y. R. Shen and F. Wang, *Nature*, 2009, **459**, 820–823.
37 W. Song, C. He, W. Zhang, Y. Gao, Y. Yang, Y. Wu, Z. Chen, X. Li and Y. Dong, *Carbon*, 2014, **77**, 1020–1030.
38 S. Pei and H.-M. Cheng, *Carbon*, 2012, **50**, 3210–3228.
39 H. Shi, C. Wang, Z. Sun, Y. Zhou, K. Jin, S. A. T. Redfern and G. Yang, *Opt. Express*, 2014, **22**, 19375–19385.
40 G. Muruganandi, M. Saravanan, G. Vinitha, M. B. Jessie Raj and T. C. Sabari Girisun, *Chem. Phys.*, 2017, **488–489**, 55–61.
41 T. Remyamol, H. John and P. Gopinath, *Carbon*, 2013, **59**, 308–314.
42 T. R. Ensley and N. K. Bambha, *Opt. Express*, 2019, **27**, 37940–37951.
43 V. Kumar, D. Mandal, K. A. Sree Raj, B. Chakraborty, A. Agarwal, C. S. Rout and K. V. Adarsh, *Phys. Rev. Appl.*, 2023, **19**, 44081.
44 M. Parishani, M. Nadafan and R. Malekfar, *RSC Adv.*, 2022, **12**, 5281–5289.
45 R. Sharma, J. Aneesh, R. K. Yadav, S. Sanda, A. R. Barik, A. K. Mishra, T. K. Maji, D. Karmakar and K. V. Adarsh, *Phys. Rev. B*, 2016, **93**, 155433.
46 V. Kumar, Afreen, S. R. KA, P. Mane, B. Chakraborty, C. S. Rout and K. V. Adarsh, *J. Phys. Chem. C*, 2023, **127**, 18485–18493.
47 B. Binish, K. M. Rahulan, T. C. S. Girisun and N. S. Panicker, *Sci. Rep.*, 2025, **15**, 2615.
48 S. Tekin, Y. Tutel, A. Karatay, H. E. Unalan and A. Elmali, *J. Lumin.*, 2022, **252**, 119362.
49 A. Doğan, A. Karatay, M. Isik, E. A. Yıldız, N. M. Gasanly and A. Elmali, *Cryst. Growth Des.*, 2024, **24**, 6981–6990.
50 K. A. A. Mary, N. V. Unnikrishnan and R. Philip, *APL Mater.*, 2014, **2**, 76104.
51 B. A. Ünlü, A. Karatay, E. A. Yildiz, T. Dinçbay, H. Ünver, N. Gasanly and A. Elmali, *J. Lumin.*, 2022, **241**, 118540.
52 A. Karatay, Y. O. Donar, A. Sınağ and A. Elmali, *Opt. Laser Technol.*, 2018, **108**, 510–514.
53 Y. Pepe, Y. Tutel, E. A. Yildiz, A. Karatay, H. E. Unalan and A. Elmali, *Adv. Eng. Mater.*, 2021, **23**, 2100468.
54 S. J. Shetty, S. S. Bhat, N. B. Gummagol, S. Surabhi and J. R. Jeong, *Carbon*, 2025, **235**, 120025.
55 M. Saravanan, T. C. Sabari Girisun, G. Vinitha and S. Venugopal Rao, *RSC Adv.*, 2016, **6**, 91083–91092.
56 Y. Pepe, S. Akkoyun, B. Bozkurt, A. Karatay, A. Ates and A. Elmali, *J. Mater. Chem. C*, 2023, **11**, 2756–2763.
57 B. A. Ünlü, D. Sener, S. Tekin, E. A. Yildiz, A. Karatay, T. Serin and A. Elmali, *Phys. Status Solidi B*, 2021, **258**, 2000539.
58 S. Chen, B. Zhu, T. Xing, J. Yang and Y. Gu, *Mater. Res. Express*, 2022, **9**, 106201.

59 D. C. Marcano, D. V. Kosynkin, J. M. Berlin, A. Sinitskii, Z. Sun, A. Slesarev, L. B. Alemany, W. Lu and J. M. Tour, *ACS Nano*, 2010, **4**, 4806–4814.
60 J. Chen, B. Yao, C. Li and G. Shi, *Carbon*, 2013, **64**, 225–229.
61 M. A. Ceniceros-Reyes, K. S. Marín-Hernández, U. Sierra, E. M. Saucedo-Salazar, R. Mendoza-Resendez, C. Luna, P. J. Hernández-Belmares, O. S. Rodríguez-Fernández, S. Fernández-Tavizón, E. Hernández-Hernández and E. D. Barriga-Castro, *Surf. Interfaces*, 2022, **35**, 102448.
62 Y. Liang and B. Fang, *Mater. Res. Bull.*, 2013, **48**, 4118–4124.
63 B. K. Sahu and A. Das, *J. Alloys Compd.*, 2020, **834**, 154901.
64 M. Sheik-Bahae, A. A. Said and E. W. Van Stryland, *Opt. Lett.*, 1989, **14**, 955–957.
65 M. Sheik-Bahae, A. A. Said, T.-H. Wei, D. J. Hagan and E. W. Van Stryland, *IEEE J. Quantum Electron.*, 1990, **26**, 760–769.
66 E. Koushki, A. Farzaneh and S. H. Mousavi, *Appl. Phys. B:Lasers Opt.*, 2010, **99**, 565–570.
67 C. H. Kwak, Y. L. Lee and S. G. Kim, *J. Opt. Soc. Am. B*, 1999, **16**, 600–604.
68 R. Karimzadeh, H. Aleali and N. Mansour, *Opt. Commun.*, 2011, **284**, 2370–2375.
69 Q. Li, R. Wang, F. Xu, X. Wang, Z. Yang and X. Gai, *Opt. Mater. Express*, 2020, **10**, 1413–1420.
70 M. Yin, H. P. Li, S. H. Tang and W. Ji, *Appl. Phys. B:Lasers Opt.*, 2000, **70**, 587–591.
71 F. L. S. Cuppo, A. M. F. Neto, S. L. Gómez and P. Palffy-Muhoray, *J. Opt. Soc. Am. B*, 2002, **19**, 1342–1348.
72 M. D. Zidan and A. Allahham, *Optoelectron. Lett.*, 2024, **20**, 177–182.
73 G. Tsigaridas, P. Persephonis and V. Giannetas, *Mater. Sci. Eng., B*, 2009, **165**, 182–185.
74 T. Ahmed, P. Das Gupta, Z. H. Khan, S. F. Uddin Farhad, H. Das, Z. T. Rakhy, N. Tasnim, A. Habib, A. I. Talukder and M. Wahadoszamen, *Opt. Mater.*, 2025, **159**, 116599.
75 P. Aloukos, I. Papagiannouli, A. B. Bourlinos, R. Zboril and S. Couris, *Opt. Express*, 2014, **22**, 12013–12027.
76 J. P. Gordon, R. C. C. Leite, R. S. Moore, S. P. S. Porto and J. R. Whinnery, *J. Appl. Phys.*, 1965, **36**, 3–8.
77 S. J. Sheldon, L. V. Knight and J. M. Thorne, *Appl. Opt.*, 1982, **21**, 1663–1669.
78 C. A. Carter and J. M. Harris, *Appl. Opt.*, 1984, **23**, 476–481.
79 J. R. Whinnery, *Acc. Chem. Res.*, 1974, **7**, 225–231.
80 B. Gu, W. Ji, P. S. Patil, S. M. Dharmaprakash and H.-T. Wang, *Appl. Phys. Lett.*, 2008, **92**, 91118.
81 G. Kresse and J. Hafner, *Phys. Rev. B:Condens. Matter Mater. Phys.*, 1993, **47**, 558–561.
82 G. Kresse and J. Hafner, *Phys. Rev. B:Condens. Matter Mater. Phys.*, 1994, **49**, 14251–14269.
83 G. Kresse and J. Furthmüller, *Comput. Mater. Sci.*, 1996, **6**, 15–50.
84 G. Kresse and J. Furthmüller, *Phys. Rev. B:Condens. Matter Mater. Phys.*, 1996, **54**, 11169–11186.
85 J. P. Perdew, K. Burke and M. Ernzerhof, *Phys. Rev. Lett.*, 1996, **77**, 3865–3868.
86 P. E. Blöchl, *Phys. Rev. B:Condens. Matter Mater. Phys.*, 1994, **50**, 17953–17979.
87 H. J. Monkhorst and J. D. Pack, *Phys. Rev. B*, 1976, **13**, 5188–5192.
88 S. Grimme, *J. Comput. Chem.*, 2006, **27**, 1787–1799.
89 M. Feng, H. Zhan and Y. Chen, *Appl. Phys. Lett.*, 2010, **96**, 33107.
90 S. Yang, W. Yue, D. Huang, C. Chen, H. Lin and X. Yang, *RSC Adv.*, 2012, **2**, 8827–8832.
91 C. Zhu, S. Guo, Y. Fang and S. Dong, *ACS Nano*, 2010, **4**, 2429–2437.
92 H. Ragupathi, M. Jarvin, S. S. R. Inbanathan, A. K. Nayak and Y. Choe, *New J. Chem.*, 2023, **47**, 4644–4655.
93 M. C. Shibu, M. D. Benoy, S. Shanavas, J. Duraimurugan, G. Suresh Kumar, M. Abu Haija, P. Maadeswaran, T. Ahamad, Q. Van Le and S. M. Alshehri, *Chemosphere*, 2022, **307**, 136105.
94 J. Li, C. Chen, J. Li, S. Li and C. Dong, *J. Mater. Sci. Mater. Electron.*, 2020, **31**, 16539–16547.
95 M. Niederberger and N. Pinna, *Metal oxide nanoparticles in organic solvents: synthesis, formation, assembly and application*, Springer Science & Business Media, 2009.
96 A. Inayat, M. Faizan, I. Ullah, A. Haider, K.-W. Nam, J.-Y. Kim, M. Alam and S. Mustansar Abbas, *J. Electroanal. Chem.*, 2023, **951**, 117903.
97 B. K. Sahu, R. N. Juine, M. Sahoo, R. Kumar and A. Das, *Chemosphere*, 2021, **276**, 130142.
98 B. K. Sahu, A. Das, A. K. Prasad and G. Mangamma, *J. Nanosci. Nanotechnol.*, 2019, **19**, 7764–7770.
99 K. Sakamoto, D. Tokunaga, S. Itoh, H. Hidai, S. Matsusaka, T. Omatsu, K. Koyama, S.-W. Kim and N. Morita, *Diamond Relat. Mater.*, 2023, **136**, 110045.
100 Aarti, A. Gaur, P. Chand, J. Shah and R. K. Kotnala, *ACS Omega*, 2022, **7**, 43647–43656.
101 Y. Wang, J. Ding, Y. Liu, Y. Liu, Q. Cai and J. Zhang, *Ceram. Int.*, 2015, **41**, 15145–15152.
102 E.-S. M. Duraia, S. Das and G. W. Beall, *Sens. Actuators, B*, 2019, **280**, 210–218.
103 Y. Wang, Y. Liu and J. Zhang, *J. Nanopart. Res.*, 2015, **17**, 420.
104 M. D. Zidan, A. W. Allaf, A. Allahham and A. Alzier, *Optik*, 2020, **200**, 163175.
105 R. Karimzadeh and N. Mansour, *Opt. Laser Technol.*, 2010, **42**, 783–789.
106 V. S. Zanuto, J. F. M. dos Santos, M. L. Baesso and T. Catunda, *Opt. Laser Technol.*, 2021, **142**, 107248.
107 S. Jeyaram and T. Geethakrishnan, *J. Mater. Sci. Mater. Electron.*, 2017, **28**, 9820–9827.
108 F. Z. Henari, *J. Opt. A:Pure Appl. Opt.*, 2001, **3**, 188.
109 M. Bala Murali Krishna, N. Venkatramaiah, R. Venkatesan and D. Narayana Rao, *J. Mater. Chem.*, 2012, **22**, 3059–3068.
110 P. Burkins, R. Kuis, I. Basaldua, A. M. Johnson, S. R. Swaminathan, D. Zhang and S. Trivedi, *J. Opt. Soc. Am. B*, 2016, **33**, 2395–2401.
111 M. Yue, J. Si, L. Yan, Y. Yu and X. Hou, *Opt. Mater. Express*, 2018, **8**, 698–703.

112 B. Yu, G. Zhang, G. Tang, X. Wu, W. Chen, B. Yang and P. Zhao, *Acta Phys. Sin.*, 1996, **5**, 377.
113 M. H. Majles Ara, P. Boroojerdian, Z. Javadi, S. Zahedi and M. Morshedian, *Optik*, 2012, **123**, 2090–2094.
114 W. Ma, Z. Li, H. Cao, L. Liang, H. Lu, Y. Liu and Y. Song, *Opt. Express*, 2023, **31**, 6252–6261.
115 K. Kumara, V. S. Kindalkar, F. Jyothi Serrao, T. Chandra Shekhara Shetty, P. S. Patil and S. M. Dharmaprakash, *Mater. Today: Proc.*, 2022, **55**, 186–193.
116 B. Zhu, F. Wang, P. Li, C. Wang and Y. Gu, *Phys. Chem. Chem. Phys.*, 2018, **20**, 27105–27114.
117 N. Venkatram, R. Sathyavathi and D. N. Rao, *Opt. Express*, 2007, **15**, 12258–12263.
118 T. Ahmed, P. Das Gupta, Z. Hasan Khan, H. Das, T. Akbar Faruquee, M. Alam Bhuiyan, S. Farid Uddin Farhad, I. M. Syed, A. I. Talukder and M. Wahadoszamen, *Results Phys.*, 2024, **64**, 107889.
119 Y. Yuan, B. Zhu, F. Cao, J. Wu, Y. Hao and Y. Gu, *Results Phys.*, 2021, **27**, 104568.
120 S. Molakkalu Padre, S. J. Shetty, S. S. Bhat, D. G. Rebello, S. Surabhi, S. Rao, N. B. Gummagol, M. R. Waikar, R. G. Sonkawade and G. S. Chandrasekhar, *ACS Omega*, 2024, **9**, 46773–46783.
121 K. Kumara, T. C. S. Shetty, S. R. Maidur, P. S. Patil and S. M. Dharmaprakash, *Optik*, 2019, **178**, 384–393.
122 Y. Huang, J. Wang, B. Bai, M. Zhao, X. Zhen, L. Zhao, X. Zhai, L. Zhao and X. Leng, *ACS Appl. Mater. Interfaces*, 2024, **16**, 59022–59029.
123 Y. Yu, J. Si, L. Yan, M. Li and X. Hou, *Carbon*, 2019, **148**, 72–79.
124 Y. Ge, J. Tan, G. Xu, X. Feng, E. Li, Y. Wang, C. Lu and X. Xu, *ACS Nano*, 2024, **18**, 30838–30847.
125 B. Chen, Q. Ouyang, L. Chen, H. Huang, Z. Chen, J. Pan, X. Fang and B. Zhang, *J. Mater. Chem. C*, 2024, **12**, 4501–4510.
126 A. Alice Noble, I. H. Joe and S. Nazar, *Carbon*, 2024, **228**, 119435.
127 M. Yüksek, U. Kürüm, H. G. Yaglioglu, A. Elmali and A. Ateş, *J. Appl. Phys.*, 2010, **107**, 33115.
128 Y. Pepe, S. Akkoyun, N. Asci, E. Cevik, Y. Tutel, A. Karatay, H. E. Unalan and A. Elmali, *ACS Omega*, 2023, **8**, 47954–47963.
129 Y. Pepe, E. A. Yildiz, M. Isik, A. Karatay, N. Gasanly and A. Elmali, *Phys. Scr.*, 2023, **98**, 75922.
130 Y. Pepe, E. Cevik, Y. Tutel, A. Karatay, H. E. Unalan and A. Elmali, *Mater. Chem. Phys.*, 2023, **309**, 128452.
131 P. Kumbhakar, A. K. Kole, C. S. Tiwary, S. Biswas, S. Vinod, J. Taha-Tijerina, U. Chatterjee and P. M. Ajayan, *Adv. Opt. Mater.*, 2015, **3**, 828–835.
132 A. Salah, A. Mansour, M. B. Mohamed, I. M. Azzouz, S. Elnaby and Y. Badr, *Appl. Surf. Sci.*, 2015, **353**, 112–117.